V+ 2 Technical Manual Series: Eye Dosimetry Module

December 2024

Renaissance Code Development, LLC
310 NW 5th St., Suite 203
Corvallis, Oregon 97330
(541) 286-4428
http://www.rcdsoftware.com

Preparer:	David Hamby	DN: cn=David Hamby, o=Renaissance Code Development, ou=Operations Manager, email=david.hamby@rcdsoftware.com, c=US Date: 2025.03.27 15:03:18 -07'00'
Reviewer:	Jeffrey Luitjens	cn=Jeffrey Luitjens, o=Renaissance Code Development, ou=Director - Software Division, email=jeff.luitjens@rcdsoftware.com, c=US 2025.03.28 13:47:25 -07'00'
Approver:	Roland R. Benke	DN: cn=Roland R. Benke, o=Renaissance Code Development, ou=General Manager, email=roland.benke@rcdsoftware.com, c=US Date: 2025.03.28 19:06:21 -05'00'

ABSTRACT

VARSKIN+ is a U.S. Nuclear Regulatory Commission (NRC) computer code originally used by staff members and NRC licensees to calculate occupational dose to the skin resulting from exposure to radiation emitted from hot particles or other contamination on or near the skin. These assessments are required by Title 10 of the *Code of Federal Regulations* (10 CFR) 20.1201(c). In addition to skin contamination, NRC staff evaluate dose estimates to the lens of the eye from various exposure scenarios. This document provides the V+ user with the technical basis for dosimetry calculations in the EyeDose Module.

Table of Contents

LIST OF FIGURES

LIST OF TABLES

ACKNOWLEDGMENTS

This report documents the work performed by Renaissance Code Development, LLC (RCD) for the U.S Nuclear Regulatory Commission (NRC) under Contract No. 31310022C0011. Staff at the Pacific Northwest National Laboratory authored initial versions of VARSKIN (US NRC 1987; US NRC 1989), with later versions amended at Colorado State University (US NRC 1992), the Center for Nuclear Waste Regulatory Analyses (US NRC 2006), and Oregon State University (US NRC 2011; US NRC 2014; US NRC 2018). RCD performed the activities described herein on behalf of the NRC Office of Nuclear Regulatory Research, Division of Systems Analysis. This report is a product of RCD and does not necessarily reflect the views or regulatory position of the NRC.

The authors are indebted to S. Bush-Goddard, B. Allen, R. Flora, J. Tomon, V. Shaffer, M. Saba, and S. Sherbini for their lasting support during development and maintenance of many of the dosimetry models now appearing in VARSKIN+.

1.0 INTRODUCTION

EyeDose allows for the evaluation of photon and electron dose to the total lens of the human eye for radionuclides in the ICRP 38 or ICRP 107 database or for monoenergetic sources. The source of photons and electrons is assumed to be on-axis with the eyeball (i.e., the exposed individual is staring at the source) and the lens dose is calculated for both unshielded and shielded eyes. Shielding is provided by standard safety glasses containing 2 mm leaded glass (Spackman 2013). Figure 1-1 presents the single user interface for accepting inputs and displaying simulation results.

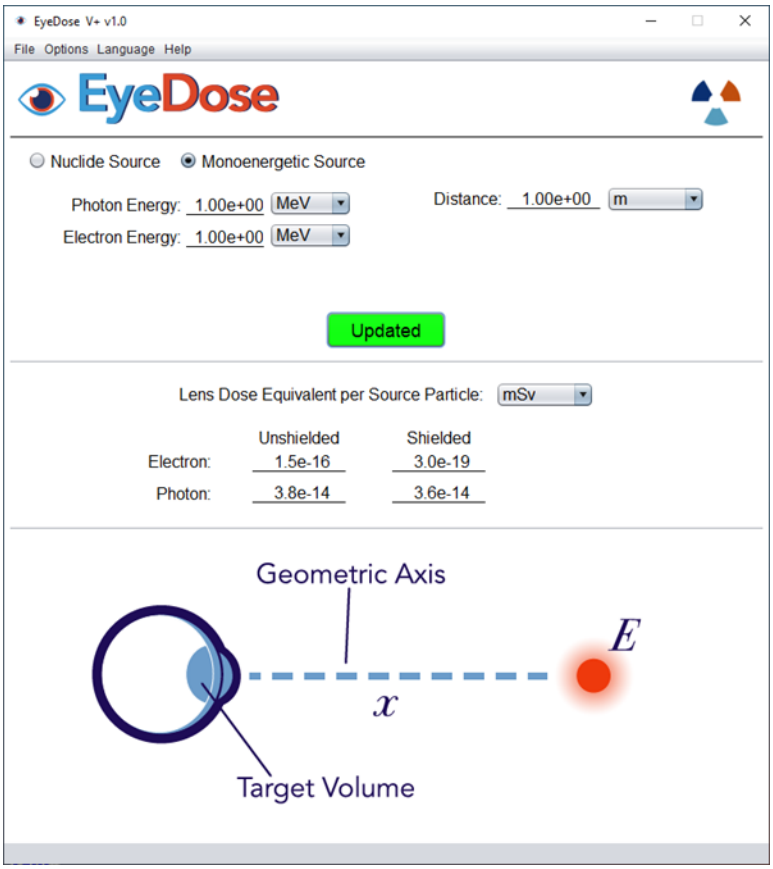

Figure 1-1 The EyeDose User Interface

EyeDose calculates dose to the whole lens as shielded and unshielded. Unshielded dose assumes a direct path from the source to the surface of the eyeball. Shielded dose refers to dose equivalent to the lens of the eye after incoming radiation has been attenuated by a standard pair of 2 mm safety glasses (Spackman 2013). The glass is assumed to be centered around the eye while still resting on the nose. The safety glass begins at a fixed value of 1.05 cm from the surface of the eye. Therefore, EyeDose will report “N/A” for shielded dose if the distance between source and eyeball is less than or equal to 1.25 cm. The user

should remember that when dealing with higher energy photons, it is possible that the shielded dose equivalent is higher than the unshielded due to attenuation, buildup, and redirection.

Another unique EyeDose feature is from the “Monoenergetic Source” selection. With an assumption of a monoenergetic incident beam, it is not feasible to return a dose as a function of exposure time. EyeDose instead returns the dose equivalent per source particle (e.g., mSv/particle). The user must then determine the number of source particles dictated by the scenario, and manually calculate total dose. Dose equivalent can be displayed in the units of Sievert and rem, with a variety of unit prefixes.

This document describes the mathematical functions derived from thousands of MCNP scenario executions (Boozer 2020) for photon and electron exposures to the eyeball.

2.0 EYE DOSIMETRY MODEL

In the VARSKIN+ eye dose model, a set of deterministic equations were developed from a vast array of probabilistic simulations to estimate radiation dose to the lens of the eye. The V+ EyeDose module allows the user to quickly assess dose to the whole lens considering particle type (electrons or photons), particle energy, relative source distance from the eye, source emission rate, and the presence or absence of protective eyewear.

The functions used in EyeDose were developed through Monte Carlo simulations of monoenergetic radioactive sources placed at varying distances from a stylized eye model. The functions are valid for electron energies ranging from 10 keV to 11 MeV, photon energies ranging from 7 keV to 11 MeV, and source-to-eye distances of 0 to 20 meters for unshielded configurations and 1.25 cm to 20 meters for shielded configurations. Additionally, sources emitting particles over a spectrum of varying energies, such as beta emitters, have been incorporated into this new dosimetry model.

The source in EyeDose is modeled as an infinitely small, isotropic point source of energy E. As seen in Figure 2-1, the source is located on the geometric axis of the eye, with a distance r between the source and the surface of the eyeball. The target volume is taken to be the entire lens.

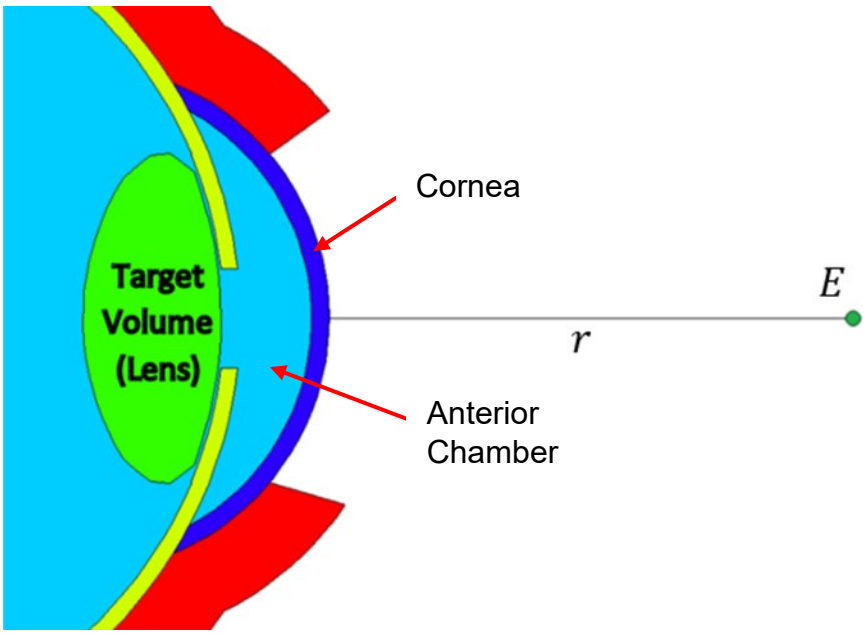

Figure 2-1. Eye Lens Arrangement Illustrating the Geometic Parameters of the Eye Dosimetry Model.

2.1. Photon Dosimetry

The development of the photon model begins with the uncollided fluence, Φ^0, as in [2.1],

$$\Phi^0(r) = \frac{S_0}{4\pi r^2}, \quad [2.1]$$

where S_0 is the source strength and r is distance between source and receptor. The fundamental equation for absorbed dose, D^0, to a point in space at distance r from an isotropic source of uncollided photons is [2.2]:

$$D^0(r,E) = E\ \Phi^0(r)\ \frac{\mu_{en}}{\rho}\ B\ e^{-\mu r}. \quad [2.2]$$

with initial energy, E, mass absorption coefficient, $\frac{\mu_{en}}{\rho}$, photon buildup factor, B, and linear attenuation coefficient, μ. Interaction-dependent variables are specific to the material through which photons are traveling.

The lens, however, is a complex volume and not a single point. The probabilistic modeling software MCNP (LANL 2003) was used to determine dose to the whole human lens over a range of photon energies after passing through and scattering in air and the cornea. The resulting form of the empirical function assumed for determining lens dose from photons of energy E emanating from an isotropic source at distance r, is [2.3]

$$D_{\mathrm{p}}(r,E) = \frac{\exp(-\mu r)}{tr^2 + ur + v}. \quad [2.3]$$

The parameters t, u, and v describe the overall shape of the function and μ is the mass attenuation coefficient Yin air. All four parameters are energy dependent. Equation [2.3] is a function of both distance and energy, with r explicitly stated and E implicit in the four parameters.

Data for mass attenuation in air are obtained from the NIST database of X-ray mass attenuation coefficients (NIST 2004). An empirical function was derived and is valid for photon energies between 3 keV and 20 MeV. The mass attenuation coefficient for air can be described by

$$\left(\frac{\mu}{\rho}\right)_{\text{air}} = \frac{\alpha_0 + \sum_{i=1}^{6} \alpha_i \ln^i E}{1 + \sum_{i=1}^{6} \beta_i \ln^i E}, \quad [2.4]$$

where ρ_{air} = 1.205x10^{-3} g cm^{-3} is the density of dry air at sea level and room temperature (i.e., 20°C). Table 2-1 provides the coefficients of Eq. [2.4].

Table 2-1. Coefficients for the Mass Attenuation Coefficient for Photons in Air Empirical Formula

Subscript i	α_i	β_i
0	6.35455E-02	-
1	3.38929E-03	5.41880E-01
2	3.21001E-05	1.90162E-01
3	1.51457E-03	6.72185E-02
4	7.81438E-05	1.57391E-02
5	3.84722E-07	1.84372E-03
6	1.91620E-05	8.28629E-05

Eq.[2.3] was fitted against more than 2,500 dose calculations performed with the use of MCNP. Once a fit was completed for a given energy, the associated values for t, u, and v were recorded and plotted as a function of energy (Figure 2-2).

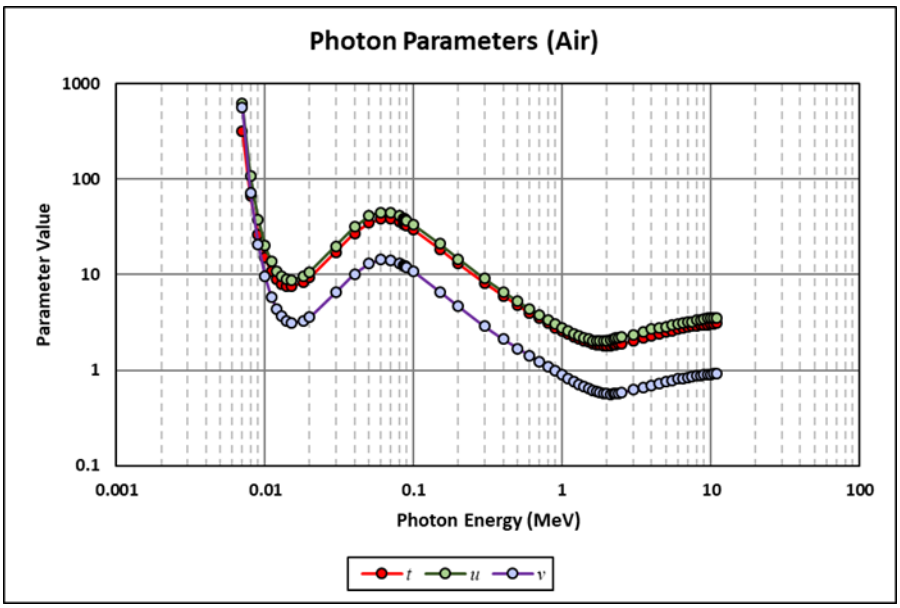

Figure 2-2. Photon Dosimetry Shaping Parameters Plotted as a Function of Energy

All three parameters plotted in Figure 2-2 were fitted against more than 720 rational functions selecting the best fit with the following results:

$$t = \exp\left[\frac{\alpha_0 + \sum_{i=1}^{5} \alpha_i \ln^i E}{1 + \sum_{i=1}^{8} \beta_i \ln^i E}\right], \quad [2.5]$$

$$u = \exp\left[\frac{\alpha_0 + \sum_{i=1}^{9} \alpha_i \ln^i E}{1 + \sum_{i=1}^{7} \beta_i \ln^i E}\right], \quad [2.6]$$

and

$$v = \exp\left[\frac{\alpha_0 + \sum_{i=1}^{9} \alpha_i \ln^i E}{1 + \sum_{i=1}^{6} \beta_i \ln^i E}\right] \quad [2.7]$$

Table 2-2 gives the coefficients of [2.5], [2.6], and [2.7].

Table 2-2. Coefficients for the Shaping Parameters in the Photon Dosimetry Model

	t	u	v
α_0	9.44146E-01	1.01867E00	-1.18618E-01
α_1	-1.35506E00	-1.54109E00	-8.16699E-01
α_2	8.64682E-01	8.89146E-01	4.50464E-01
α_3	1.85547E-01	3.76454E-01	3.71586E-02
α_4	-1.01907E-01	-1.89178E-01	-2.01271E-01
α_5	-1.97434E-02	-1.46172E-02	-3.32457E-03
α_6	-	2.48789E-02	3.51748E-02
α_7	-	-1.55929E-03	2.83451E-03
α_8	-	-2.59795E-03	-2.16321E-03
α_9	-	-3.09806E-04	-3.28384E-04
β_1	-5.72651E-01	-7.30645E-01	-3.74058E-01
β_2	2.02052E-01	-7.30645E-01	-3.74034E-02
β_3	2.28401E-01	3.75257E-01	3.71979E-01
β_4	-2.98566E-02	5.00708E-02	1.82485E-01

	t	u	v
β_5	-3.57572E-02	5.00708E-02	1.82485E-01
β_6	-2.61996E-03	-1.17824E-02	1.33298E-03
β_7	1.110680E-03	-8.96010E-04	-
β_8	1.39853E-04	-	-

Protective Glasses. The shielding used in the model is based on Spackman's "classic" style eyewear (Spackman 2013). The posterior surface of the protective lens (closest to the cornea) is assumed to be normal to the eye's geometric axis and located 1.05 cm in front of the cornea's surface. Adding the lens thickness of 2 mm places its anterior surface 1.25 cm from the cornea's exterior. To arrive at this distance, the head model used by Behrens et al. (2009) was inserted into the problem geometry and the lens was placed as close to the eye as possible without intersecting the head. The protective lenses were centered on the eye to simulate resting on the nose of the head phantom (Figure 2-3). Once the lens was placed, the head was removed from the scenario to decrease software runtime.

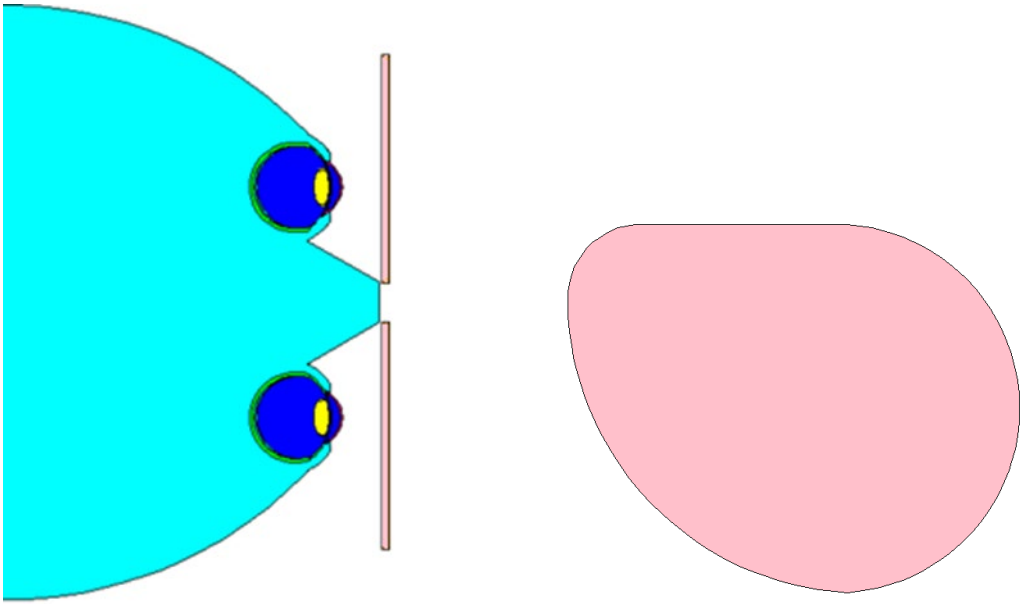

Figure 2-3. Illustration Showing Placement of the Lens Relative to the Eyes (left) and the Lens shape (right)

All parameters shown in Figure 2-4 retain their original meanings from the unshielded model (Figure 2-1). The eyewear's placement, however, requires the minimum distance between the eye and the source to be 1.25 cm.

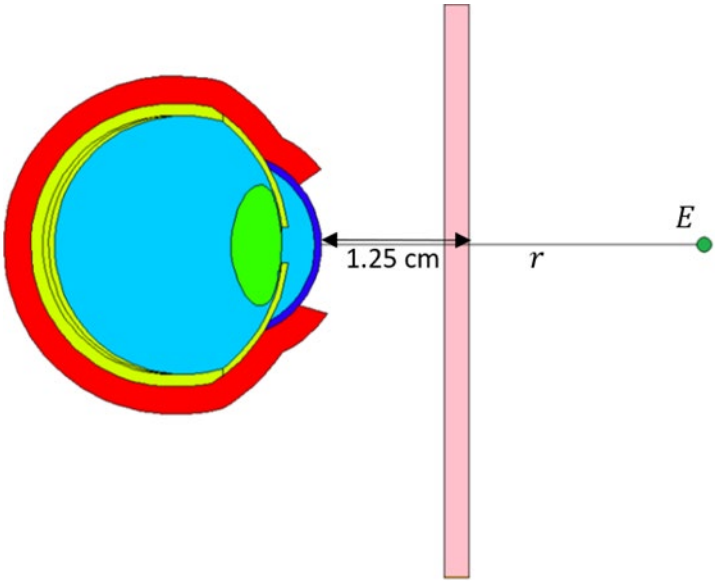

Figure 2-4. Illustration of the Geometric Parameters of the Shielded Eye

The concept of the buildup factor is extremely useful when estimating the dose after shielding has been introduced, D_{sh}. The unshielded dose will be denoted by D_{unsh}. Since the buildup factor is the ratio of total fluence to the primary fluence, total fluence can be expressed mathematically as:

$$\Phi(\mathbf{r}) = B(\mathbf{r})\Phi^0(\mathbf{r}), \qquad [2.8]$$

where $\Phi(\mathbf{r})$ is the total fluence at point $\mathbf{r}$, $\Phi^0(\mathbf{r})$ is the primary fluence at $\mathbf{r}$, and the buildup factor is $B(\mathbf{r})$. Eq. [2.8] illustrates that the total fluence can be written as a function of the primary fluence. Combining this concept with the basic equation for dose written as $D = \Phi E\left(\frac{\mu_{en}}{\rho}\right)$, shows that the dose rate at a given point is related to the fluence at that point, and so one may write:

$$D_{\mathrm{sh}}(r, E) = f\big(D_{\mathrm{unsh}}(r, E)\big). \qquad [2.9]$$

Eq. [2.9] implies that knowledge of $D_{\mathrm{unsh}}(r, E)$ is all that is needed to determine $D_{\mathrm{sh}}(r, E)$. Indeed, when shielded and unshielded dose are plotted against each other, a nearly linear relationship is discovered (see Figure 2-5). The mechanism in which photons interact with matter is highly dependent on the energy of the photon. Lower energy photons are more likely to undergo an absorption event than high-energy photons, and so shielding effectiveness tends to drop off with increasing photon energy.

Photon buildup describes the process by which the number of scatter events increases as the number of absorption events decreases. This analysis considers buildup for higher energy photons that would have otherwise missed the target but are scattered back to the target volume. At some point of increasing energy, the shielding not only stops limiting the dose to the target volume but rather begins to *increase* the dose. In Figure 2-5 the dashed black line represents the case where shielding is no longer beneficial (that is, $D_{\mathrm{sh}}(r,E) = D_{\mathrm{unsh}}(r,E)$). For leaded eyewear, this occurs around 1 MeV. Photon energies greater than 1 MeV, such as the 3 MeV trend shown in Figure 2-5, tend to deposit more energy into the target volume when shielding is present. This is not to say that leaded glasses should not be worn when E > 1 MeV. If electrons are present, their contribution may be reduced by a greater factor if protection is worn, and so protective eyewear may offer a net decrease in dose. Section 2.2 discusses electron dosimetry.

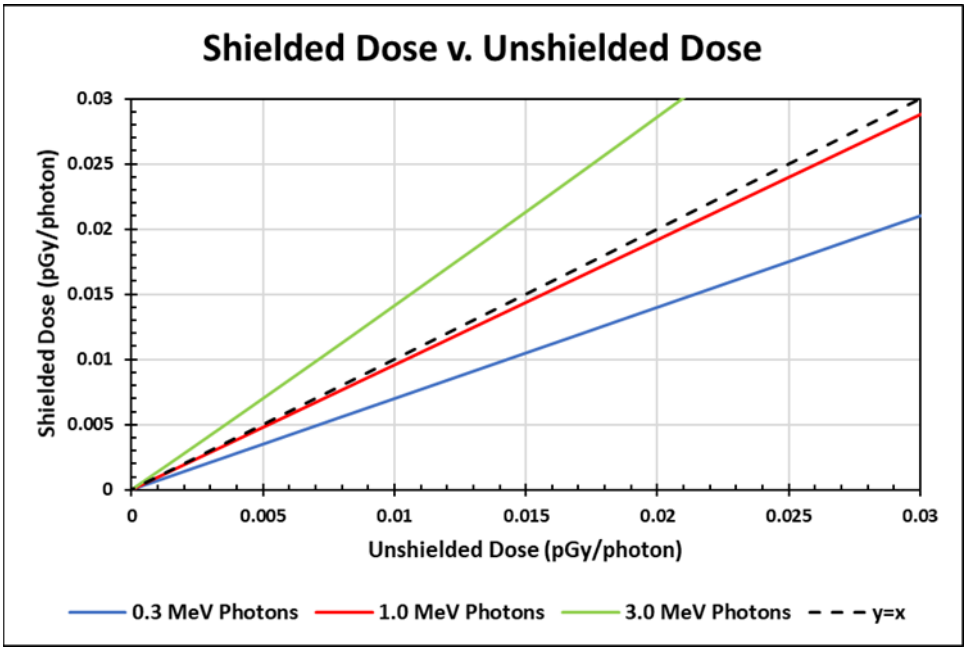

Figure 2-5. Shielded Dose Plotted as a Function of Unshielded Dose

Over 250,000 functions were tested against the data to find the best empirical fit for Eq. [2.9]. The resulting equation that best fit the data is [2.10]

$$D_{\mathrm{sh}} = AD_{\mathrm{unsh}} \exp\left(bD_{unsh} + c\sqrt{D_{unsh}}\right), \qquad [2.10]$$

where A, b, and c are energy dependent shaping parameters. In fact, A can be viewed as an indicator of the level of protection provided by the leaded glasses. Protection is afforded when A < 1. No protection is seen when $A \approx 1$ and $D_{\mathrm{sh}} > D_{\mathrm{unsh}}$ when A > 1.

Figure 2-6, which shows the mass attenuation coefficient for lead, illustrates the K-edge at 0.088 MeV. The plot shows that the probability of an interaction occurring at this energy jumps dramatically. It is because of this edge that the relationship between the shaping parameters must be split in two at 0.088 MeV. The jumps at the L-edges (< 0.02 MeV) are much smaller and no split is necessary at these energies.

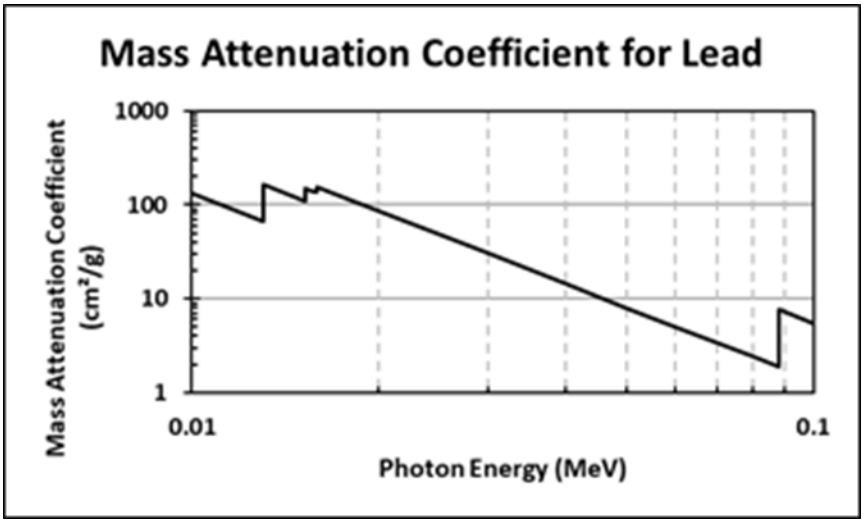

Figure 2-6. Mass Attenuation Coefficient for Lead

The relationship between the three shaping parameters of Eqs. [2.10] were determined from the analysis of 1,408 dose values calculated with MCNP, resulting in the following:

$$A = \begin{cases} \exp\left[\alpha_0 + \sum_{i=1}^{8} \alpha_i \ln^i \frac{E}{1+E}\right], & E > 0.088 \text{ MeV} \\ \exp\left[\alpha_i + \sum_{i=1}^{6} \alpha_i E^i\right], & E \leq 0.088 \text{ MeV}, \end{cases} \quad [2.11]$$

$$b = \begin{cases} \frac{\alpha_0 + \sum_{i=1}^{5} \alpha_i E^i}{1 + \sum_{i=1}^{5} \beta_{i_i} E^i}, & E > 0.088 \text{ MeV} \\ \alpha_0 + \ln\left[1 + \left(\frac{E - \alpha_1}{\alpha_2}\right)^2\right], & E \leq 0.088 \text{ MeV}, \end{cases} \quad [2.12]$$

$$c = \begin{cases} \dfrac{\alpha_0 + \sum_{i=1}^{3} \alpha_i E^i}{1 + \sum_{i=1}^{4} \beta_{i_i} E^i}, & E > 0.088 \text{ MeV} \\ \alpha_i + \sum_{i=1}^{5} \alpha_i E^i, & E \leq 0.088 \text{ MeV}. \end{cases} \quad [2.13]$$

Table 2-3 provides the values for coefficients A, b, and c. Photon energies from 7 keV to 11 MeV were tested. Energies below 50 keV yielded negligible dose and so can be taken to be zero. Equations [2.11], [2.12], and [2.13] can be used for energies between 50 keV and 11 MeV. Distances from 1.25 cm to 20 m are valid.

Table 2-3. Coefficients for the Shaping Parameters of the Shielded Dose Equation

	$E > 0.088$ MeV			$E \leq 0.088$ MeV		
	A	b	c	A	b	c
α_0	3.13591E00	-1.29037E02	4.51223E-01	-1.94542E02	1.03174E00	-1.07048E02
α_1	2.15179E01	1.00768E02	-2.23710E01	1.21618E04	9.11942E-02	9.06704E03
α_2	6.43424E01	8.33501E02	-1.34607E00	-3.36015E05	7.08353E-04	-2.88345E05
α_3	1.09630E02	-2.39218E03	1.35608E02	5.09791E06	-	4.42100E06
α_4	1.15502E02	-1.90864E03	-	-4.41170E07	-	-3.30544E07
α_5	7.69484E01	1.51367E04	-	2.04591E08	-	9.69423E07
α_6	3.15687E01	-	-	-3.94653E08	-	
α_7	7.28534E00	-	-	-	-	-
α_8	7.20570E-01	-	-	-	-	-
β_1	-	3.09273E03	-1.61930E00	-	-	-
β_2	-	-2.77860E03	-5.49709E01	-	-	-
β_3	-	-1.48815E03	3.33218E00	-	-	-
β_4	-	2.44611E02	7.32131E00	-	-	-
β_5	-	3.47614E02	-	-	-	-

2.2. Electron Dosimetry

Understanding the electron model in both shielded and unshielded circumstances first requires the analysis of the unshielded electron model in a vacuum. While the

effects of air are too important to ignore, the final model is mathematically based on the initial conditions without air.

Because bremsstrahlung plays a significant role in electron dosimetry, it must be considered. In fact, one may expect an electron point source dosimetry model to simply be the addition of the dose due to the electron source and the contribution from the bremsstrahlung source. An empirical model that fits the MCNP probabilistic data is:

$$D_{\mathrm{e}}(r,E) = \frac{\mathcal{B}^{+}(q,s)}{ar^2 + br + c\sqrt{r} + d} + \frac{\mathcal{B}^{-}(q,s)}{tr^2 + ur + v}. \qquad [2.14]$$

The parameters a, b, c, d, t, u, and v are all energy dependent shaping parameters. It was determined that adding $c\sqrt{r}$ in the first term provided a better fit for lower energy electrons.

The functions $\mathcal{B}^{+}$ and $\mathcal{B}^{-}$ are modified hyperbolic tangent functions:

$$\mathcal{B}^{-}(q,s) \equiv \frac{1}{2}[1 - \tanh q(x-s)] \qquad [2.15]$$

and

$$\mathcal{B}^{+}(q,s) \equiv \frac{1}{2}[1 + \tanh q(x-s)]. \qquad [2.16]$$

$\mathcal{B}^{-}$ and $\mathcal{B}^{+}$ are sigmoid curves that vary between 0 and 1. Each $\mathcal{B}$ is effectively a "continuous switch" that transitions between the two terms in [2.14]. The parameter q controls how quickly $\mathcal{B}$ changes from 0 to 1 and s shifts the curve left and right. Figure 2-7 shows an example of both $\mathcal{B}$ curves with q set to 1 and s set to 5.

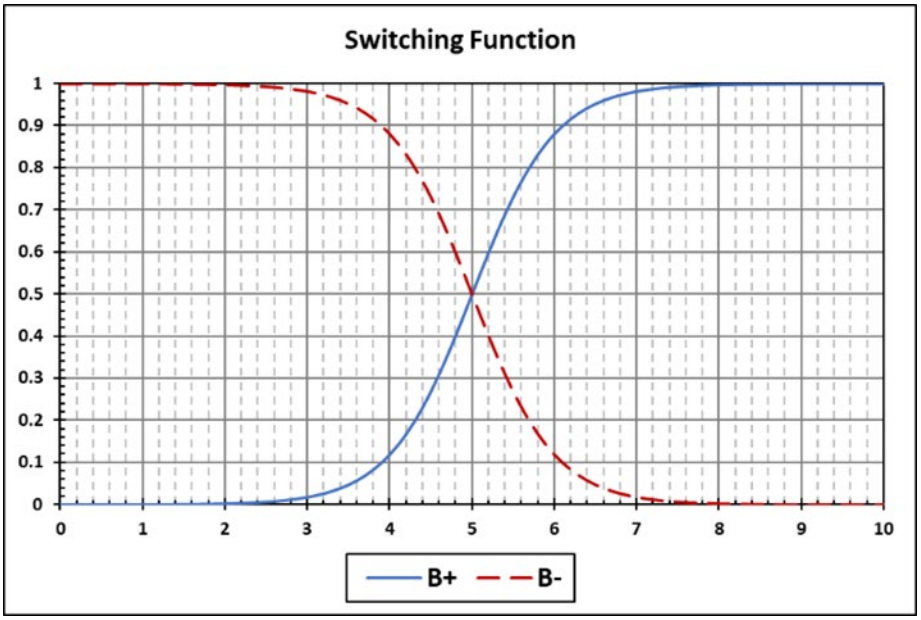

Figure 2-7. The Switching Functions $\mathcal{B}$+(q,s) and $\mathcal{B}$-(q,s) with q = 1 and s = 5

Figure 2-8 (and Figure 2-9) shows the importance of bremsstrahlung for 0.65 MeV electrons. At distances less than 0.3 cm, bremsstrahlung contributes 100 percent of the total lens dose. Electrons begin directly contributing to the total dose when $r \approx 0.3$ cm.

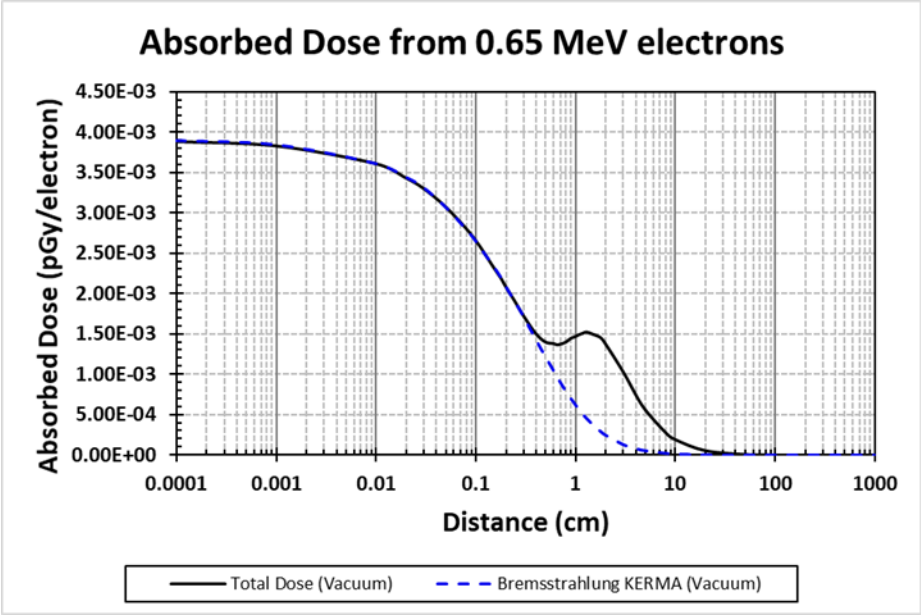

Figure 2-8. Total Dose to the Lens from 0.65 MeV Electrons (linear-log axes)

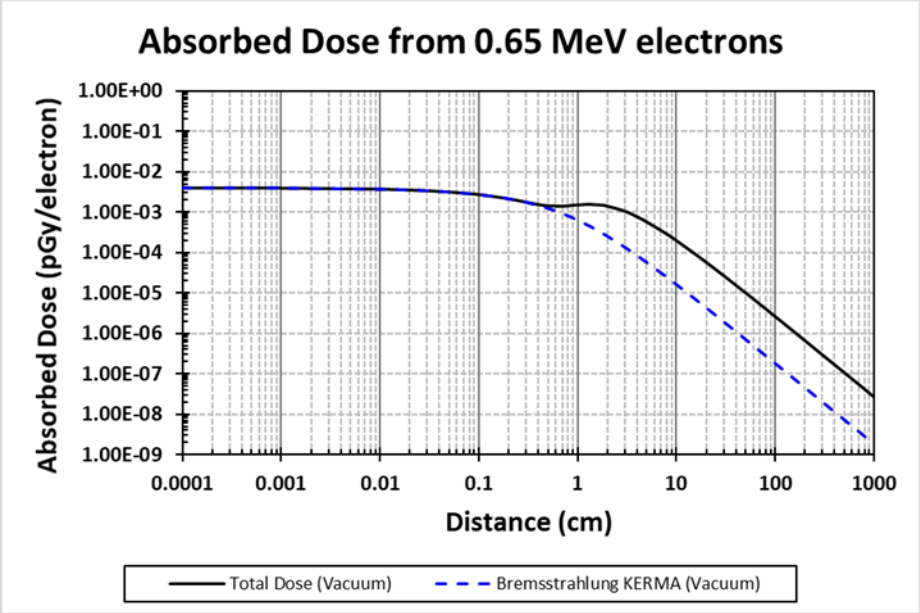

Figure 2-9 Total Dose to the Lens from 0.65 MeV Electrons (log-log axes)

The phenomena presented in the previous figures result from the shape of the eye itself. Consider Figure 2-10 which shows two cases. In the first case, the electron source is very close to the eye. The distance between the source and the lens *with the least amount of tissue* is normally incident and shown by the black arrow. Some electrons may not have enough energy to penetrate through this tissue, leaving bremsstrahlung as the only contributor to the total dose. In the second case, the electron source has been pulled back some distance. The normal route is still too thick for lower energy electrons to penetrate. However, consider the dashed purple line emanating from the source to the top of the cornea. Electrons that are incident in this region have a chance to be deflected along the second arrow. Due to the eyeball's curvature, this new path requires the electron to travel through *less* tissue before reaching the target volume. This new path is viable at around r = 0.3 cm. The electron rays radiating from the source can be considered parallel at about 10 cm, at which point both the bremsstrahlung and direct contribution obey the inverse square law.

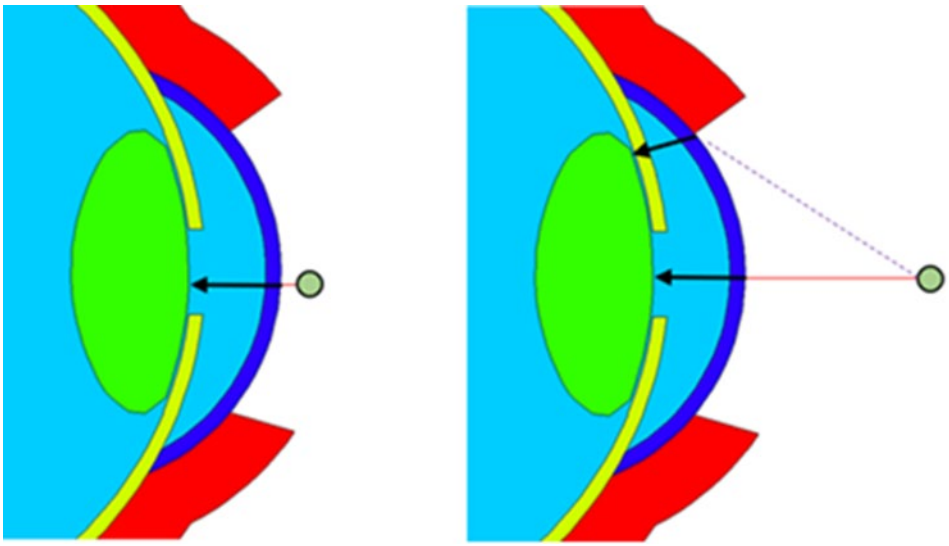

Figure 2-10. Schematic Representation of how Curved Surfaces Result in Dose from scattered Electrons

A 3rd term would seem to be needed in Eq. [2.14] to account for the scattered electron contribution. It turns out, however, that the first term can describe both the bremsstrahlung and scattered electron contributions. This allows the combination of the bremsstrahlung and scattered contributions to be modeled by a similar form as Eq. [2.14] with no attenuation in air accounted for (i.e., in a vacuum), written as:

$$D_{\mathrm{e,vac}}(r,E) = \frac{\mathcal{B}^{-}(q,s)}{ar^2+br+c\sqrt{r}+d} + \frac{\mathcal{B}^{+}(q,s)}{tr^2+ur+v}. \qquad [2.17]$$

To illustrate the effectiveness of Eq. [2.17], consider the plots for 1 and 3 MeV electrons seen in Figure 2-11 and Figure 2-12, respectively. In both cases the bremsstrahlung contribution is negligible. The 1 MeV electrons have enough energy to penetrate directly to the lens at all distances. The reduced penetration depth for r > 0.3 cm provides a pathway for the scattered dose, resulting in the odd shape seen in Figure 2-11(b). The higher energy 3 MeV electrons can easily penetrate to the target volume and the direct electron contribution dominates the shape seen in Figure 2-12 with the bremsstrahlung contribution diminished.

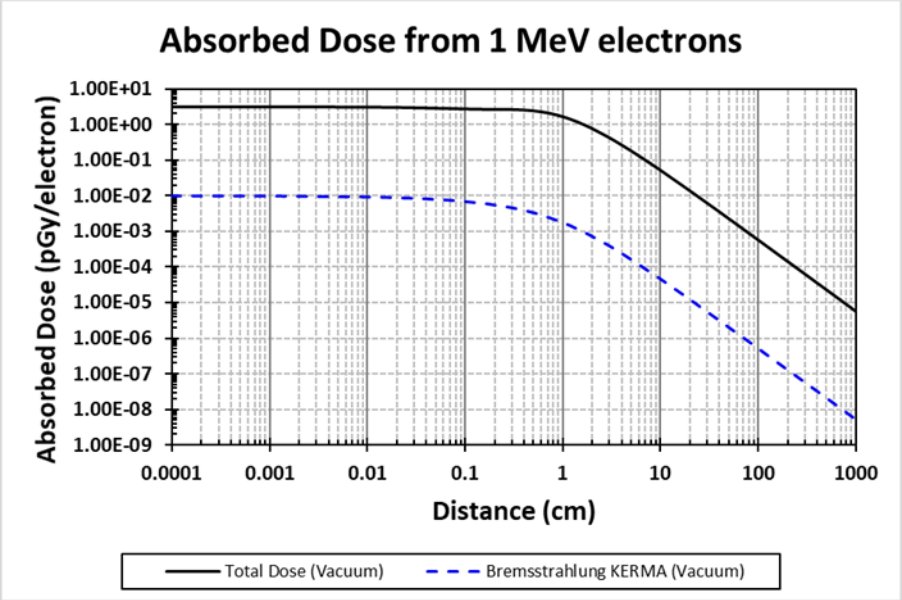

(a)

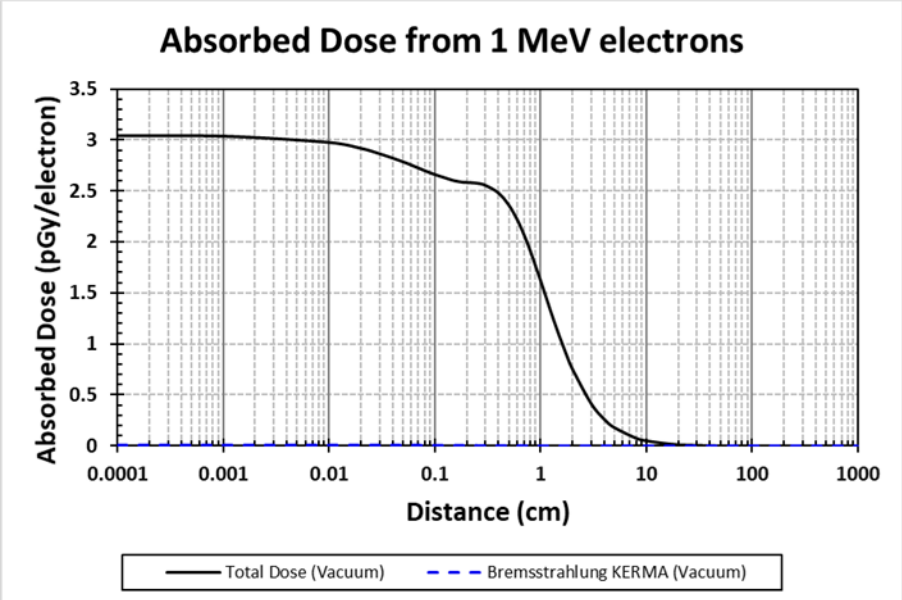

(b)

Figure 2-11. Lens Dose from 1 MeV Electrons on both (a) Linear-Log and (b) Log-Log Axes

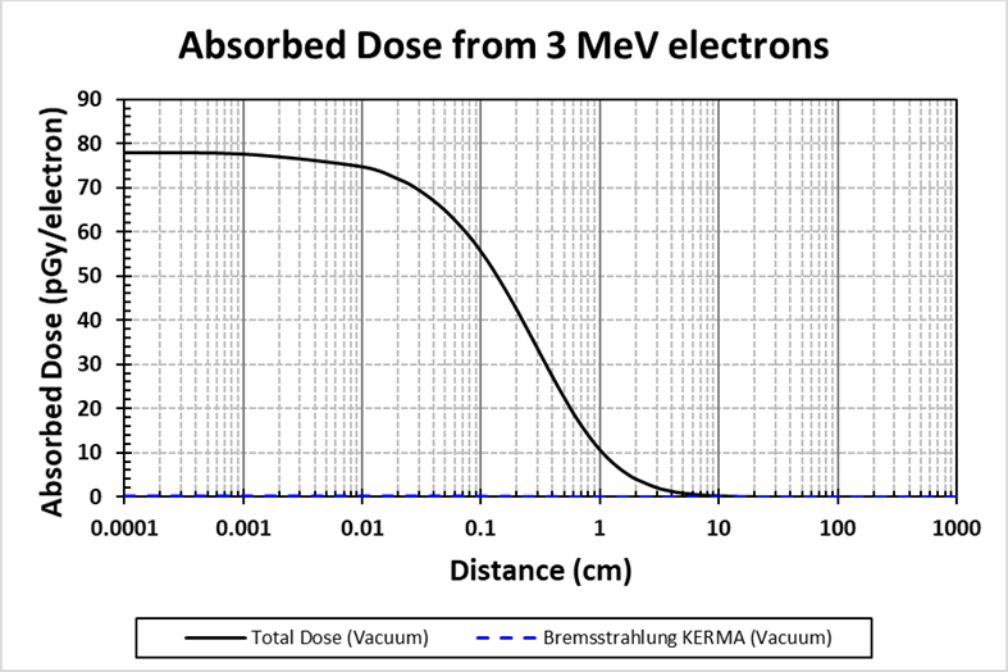

(a)

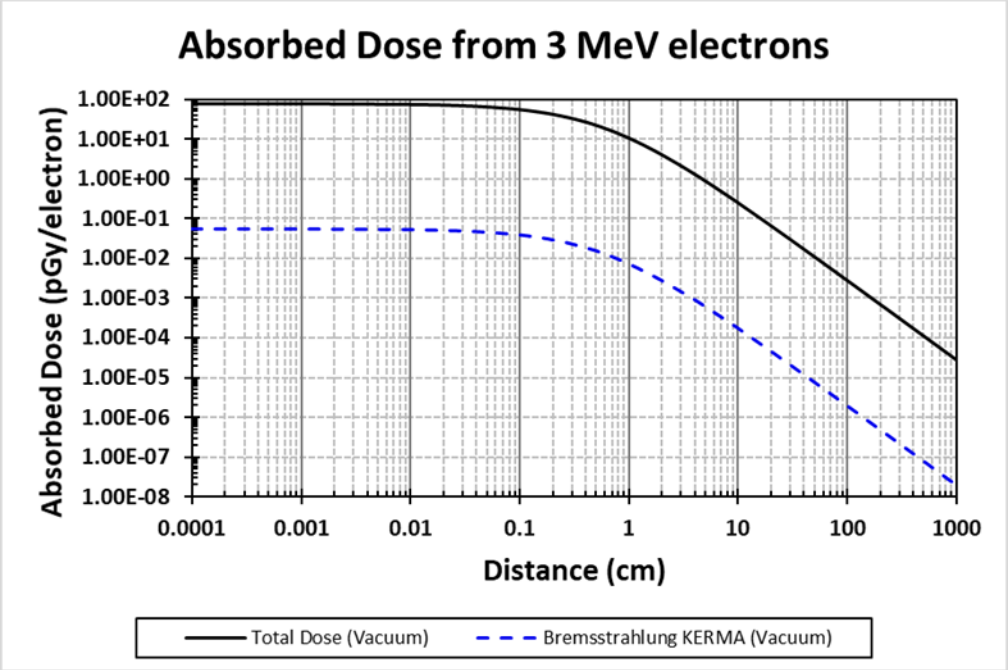

(b)

Figure 2-12. Lens Dose from 3 MeV Electrons on both (a) Linear-Log and (b) Log-Log Axes

Additional parameters to modify Eq. [2.17] are needed to account for energy degradation in air. Simplicity would suggest the following:

$$D_{\text{air}} = D_{\text{vac}} \exp(-hr) \qquad [2.18]$$

where where h behaves similarly to μ for photons. This formulation was considered but fails for purposes of this analysis for three reasons:

- The analysis concerns distances in air up to 10 m;
- The size and shape of the target volume play a significant role in electron dosimetry; and
- Bremsstrahlung generated in air is a key component of electron dose.

While traversing through space, the electron fluence undergoes dramatic transformations that are not adequately described by simple exponential decay. An empirical expression accounting for the effects of air was derived:

$$D_{\text{air}} = \frac{\mathcal{B}^{-}(q,s)}{ar^2 + br + c\sqrt{r} + d} + \frac{\mathcal{B}^{+}(q,s)\,\mathcal{B}^{-}(m,n)}{tr^2 + ur + v} + \frac{k\,\mathcal{B}^{+}(1000,z)}{(1+r)^j}. \qquad [2.19]$$

Figure 2-13 shows the absorbed dose from a point source in air and in a vacuum. There is good agreement between the two when the source is less than about 1 cm from the eye, but subtle differences begin to emerge between 1 cm and 10 cm. The two curves clearly diverge beyond 10 cm, and careful inspection of the air model indicates a bend at about 100 cm. It was discovered that $\mathcal{B}^{-}$ accurately describes the initial deviation between the vacuum and air data. The bend can be modeled by the third term in [2.19].

Equation [2.19] is further broken down by its terms in Figure 2-14. The data collected through MCNP are shown as blue dots. Each term in Eq. [2.19] is plotted separately. The dosimetry model, shown as a solid red line, is the summation of these three terms.

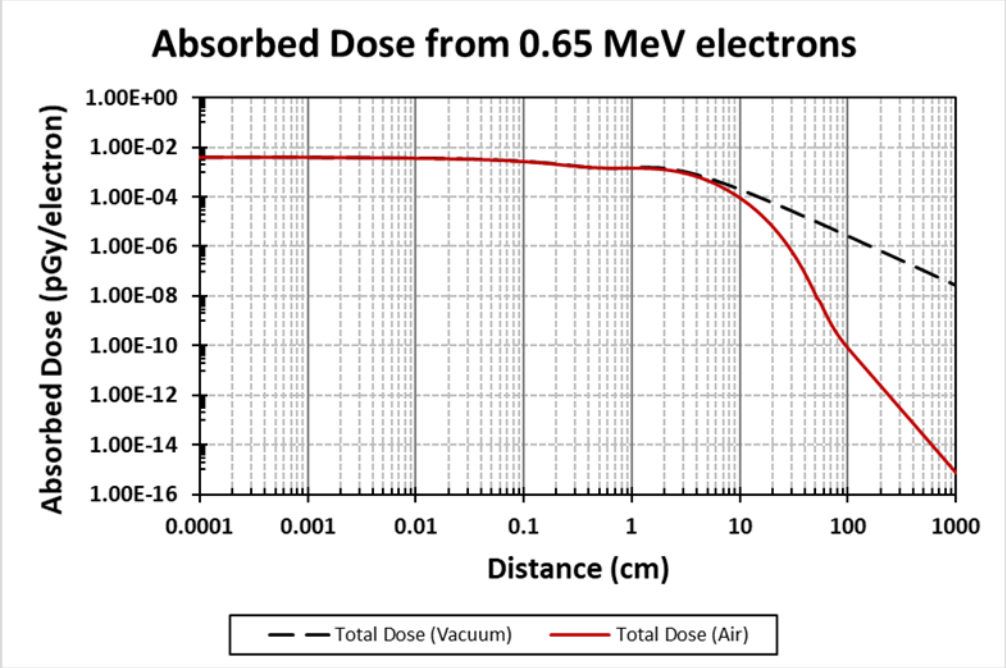

Figure 2-13 Comparison of the Dose for 0.65 MeV Electron Point Sources in Air and in Vacuum

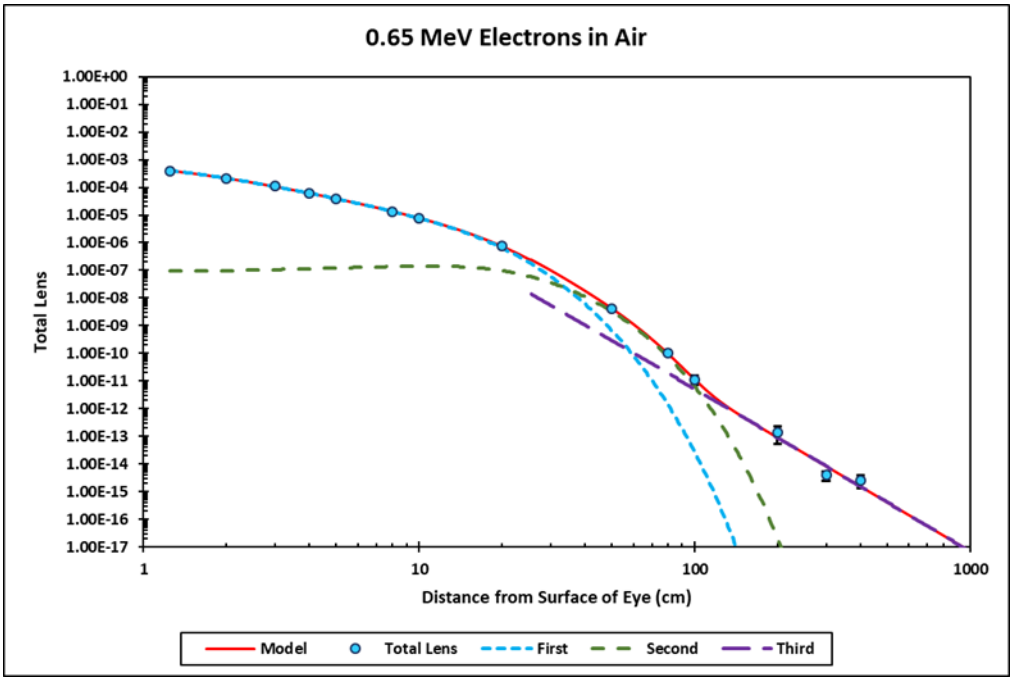

Figure 2-14 Component Breakdown of the Electron Dosimetry Model

Each term in Eq. [2.19] is a continuous differential function for $r > 0$. This implies that D_{air} must be continuous and differential as well. Equation [2.19] is a very complicated model containing 14 parameters in total. This complexity prohibits the establishment of an equation for each parameter; thus, parameter values at selected energy levels are determined at 39 points from 0.01 to 11 MeV. For requested energies between available points, the dose at the surrounding points is calculated followed by an interpolation to the specified energy.

Incorporating shielding for electrons requires a slight modification of Eq. [2.19] and recalculation of each of the shaping parameters. Similarly, the shielded electron dose model is:

$$D_{\text{sh}} = \left[\frac{\mathcal{B}^{-}(q,s)}{ar^2+br+c\sqrt{r}+d} + \frac{\mathcal{B}^{+}(q,s)\,\mathcal{B}^{-}(m,n)}{tr^2+ur+v} + \frac{k\,\mathcal{B}^{+}(1000,z)}{(1+r)^j}\right][\mathcal{B}^{-}(y,0)]. \quad [2.20]$$

Parameter values at selected energy levels are determined at 36 points from 0.08 to 11 MeV. For requested energies between available points, the dose at the surrounding points is calculated followed by an interpolation to the specified energy.

2.3. Continuous-Energy Radiation Sources

Many commonly found radioactive sources are beta emitters. These emitted beta particles are essentially high-speed electrons born from nuclear decay. Unlike gamma rays, which are radiated at discrete and predictable energies, betas are released in a continuous energy spectrum. In addition, continuous photon spectra may be encountered especially in medical and industrial settings. Equation [2.19] was developed for monoenergetic sources and is not immediately applicable to continuous sources of radiation. However, that equation is still valid with application of the following procedure.

Assume $Y(E)$ describes the continuous energy spectrum for a given source and define:

$$P(E) \equiv \frac{Y(E)}{\int Y(E)dE} \quad [2.21]$$

to represent the number of particles emitted per unit energy per disintegration. $P(E)$ is fundamentally a normalized $Y(E)$ since $P(E) = Y(E)$ if and only if $\int Y(E)dE = 1$. The product

$$D(r, E) \cdot P(E) \qquad [2.22]$$

is the lens dose per unit energy deposited by a particle of energy E at distance r. The total lens dose is found by integrating [2.22]:

$$D_{\text{total}} = \int_E D(E) \cdot P(E)dE. \qquad [2.23]$$

In the presence of discrete energy particles (such as Auger electrons, characteristic X rays or gamma rays) and continuous energy spectra (such as beta radiation or emissions from X-ray machines), Eq. [2.23] can be generalized to

$$\dot{D}_{\text{total}} = \sum_{\substack{\text{discrete}\\ \text{photons}}} A_i D_{\text{p}}(E) + \sum_{\substack{\text{continuous}\\ \text{photons}}} A_i \int_E D_{\text{p}}(E) \cdot P_i(E)dE + \sum_{\substack{\text{discrete}\\ \text{electrons}}} A_i D_{\text{e}}(E) + \sum_{\substack{\text{continuous}\\ \text{electrons}}} A_i \int_E D_{\text{e}}(E) \cdot P_i(E)dE. \qquad [2.24]$$

Above, each A_i is the emission rate for the i^{th} particle in the group. Because each A_i is an emission *rate*, Eq. [2.24] represents the total lens dose *rate*.

2.4. Verification and Validation

Photons. To illustrate how Eq. [2.3] fits the data, consider its weighted fit to 1 MeV photons (

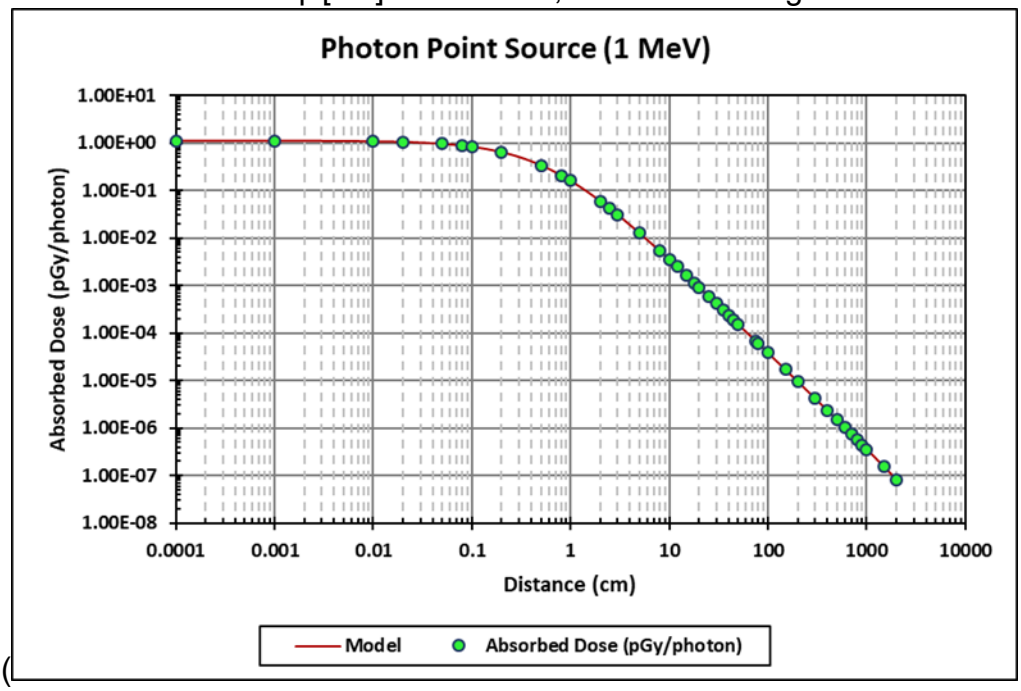

Figure 2-15). The overall shape of the function matches the data quite well, and the mean percent error (MPE) is bounded between ±0.8 percent (Figure 2-16), where the MPE is a scale-independent and unbiased measure of error between the data and the predictive model. The inverse square law predicts the photon density with respect to distance from the point source's spatial location. Points near the source will have a higher photon density than points farther from the source. The photon density is directly proportional to the number of interactions occurring in the volume, and so the number of interactions per history is expected to increase as the source is placed successively closer to the target volume. Thus, for the same number of MCNP histories, photons closer to the target volume will be associated with higher levels of certainty, and hence, higher weights. Figure 2-16 illustrates this where the MPE for r < 1 cm is less than the MPE for larger r. Figure 2-17 provides a separate indication that the model adequately represents the data over the entire range of distances.

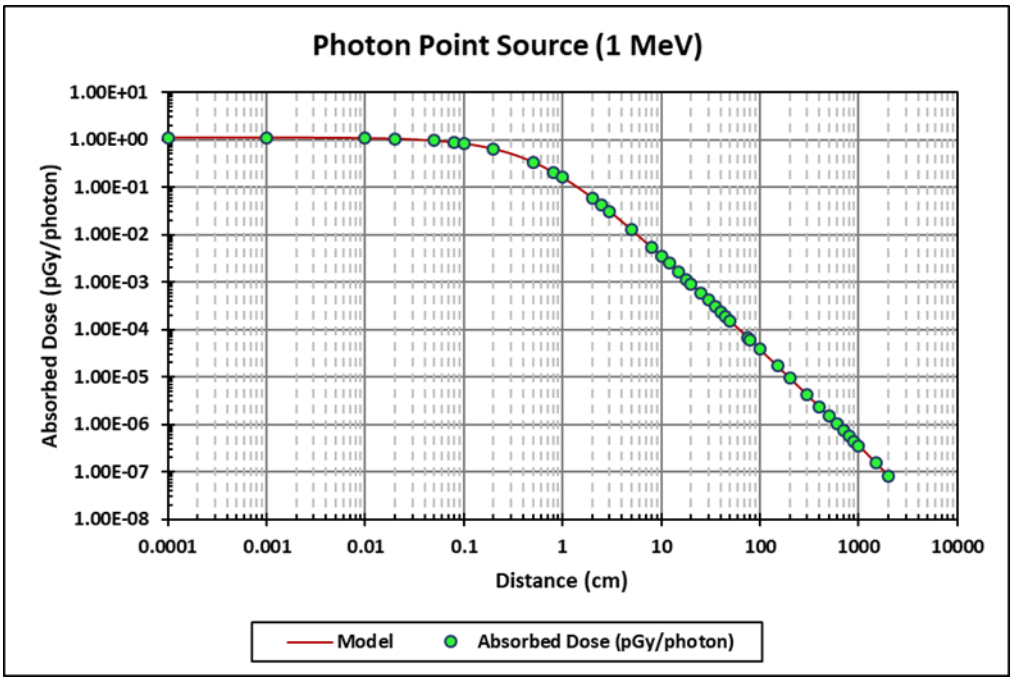

Figure 2-15. An Empirical Function Fitted Against the Absorbed Dose to the Lens for 1 MeV Photons in Air

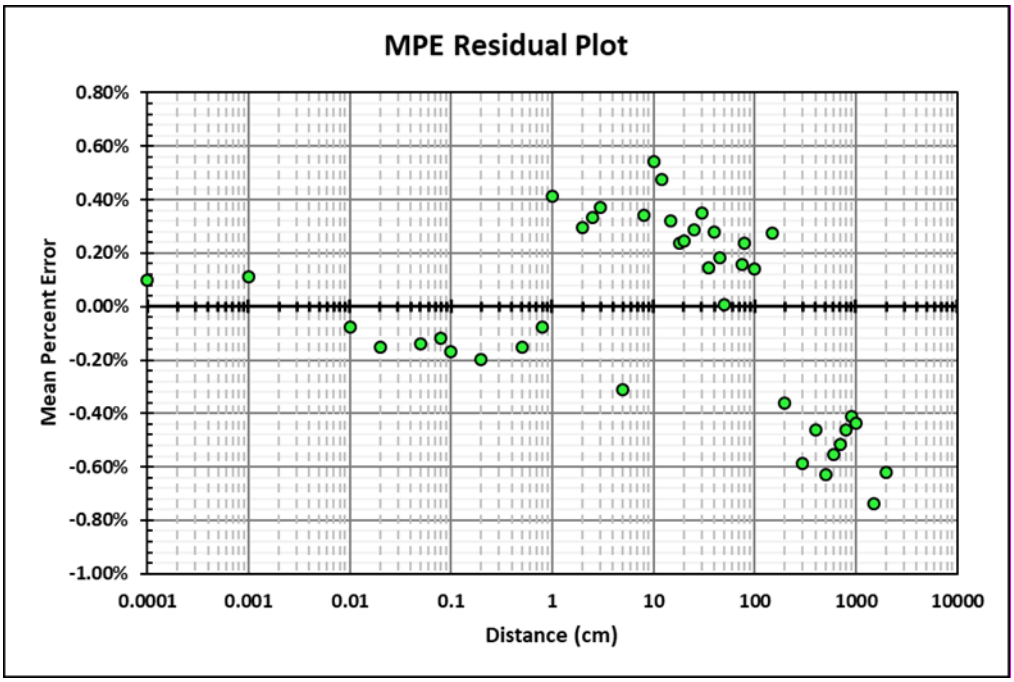

Figure 2-16. A Weighted MPE Residual Plot for the Photon Dosimetry Model Empirical Fit

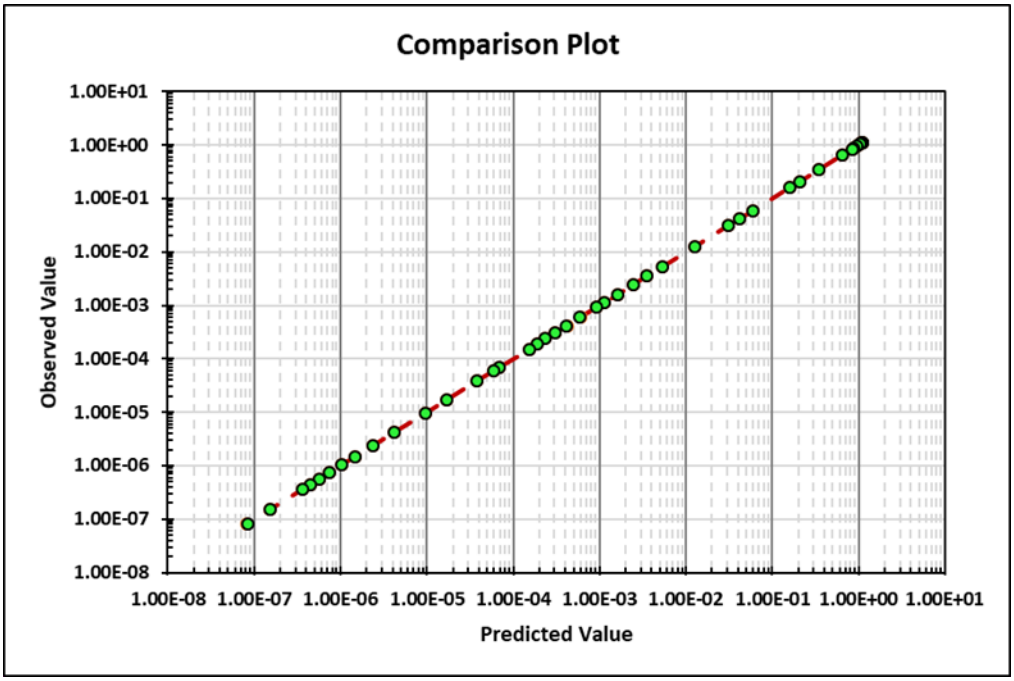

Figure 2-17. The Comparison Plot for a 1 MeV Photon Point Source

To illustrate how well Eq. [2.4] fits the data, consider

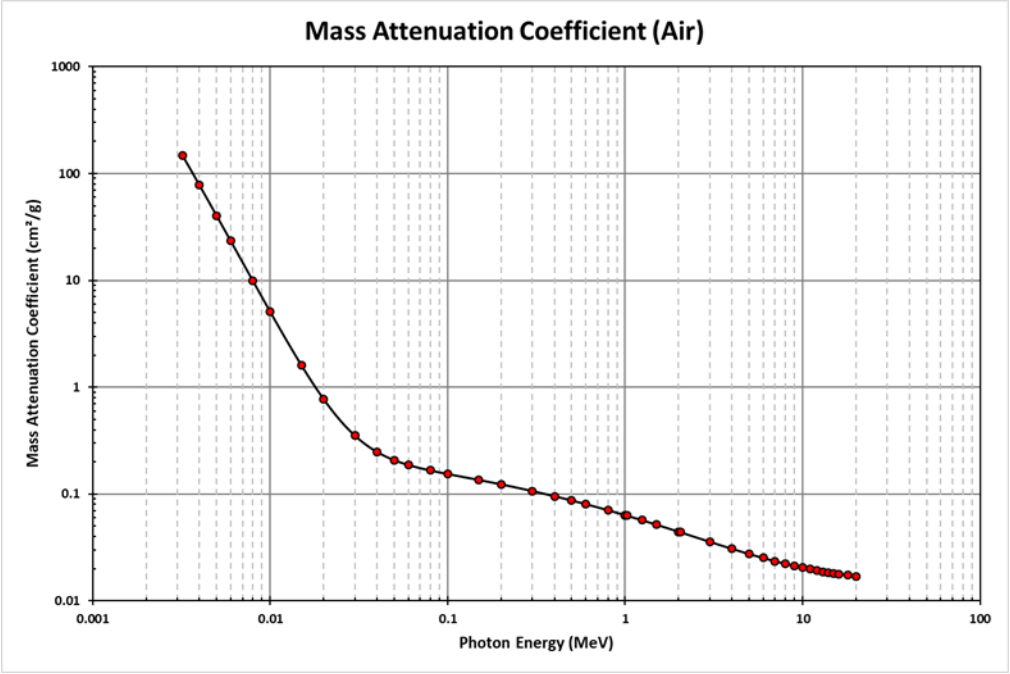

Figure 2-18 and Figure 2-19.

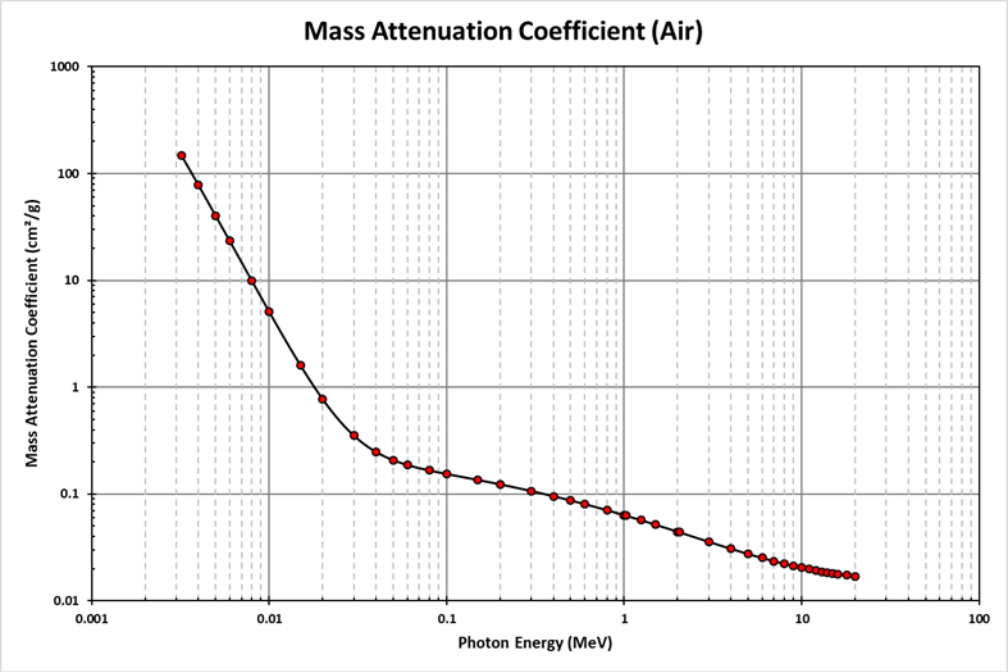

Figure 2-18 shows the empirical model overlaid on the mass attenuation data. The residual plot shown in Figure 2-19 indicates that the MPE between the function and the data is bounded by ±0.08 percent and shows no predictable pattern, indicating an excellent fit.

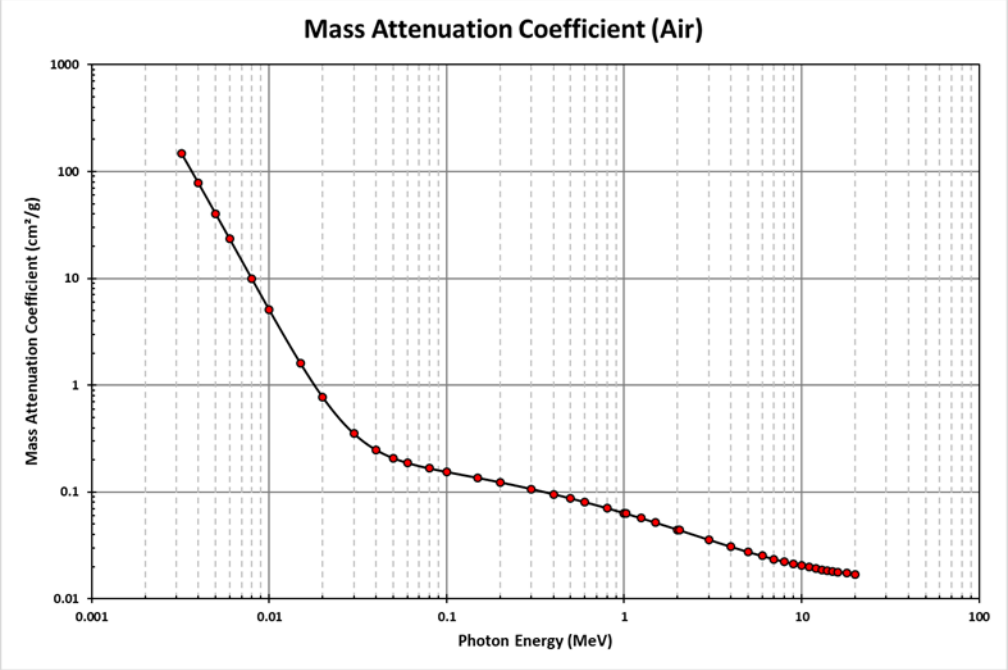

Figure 2-18. An Empirical Function Fitted Against the Mass Attenuation Coefficient for Photons in Air

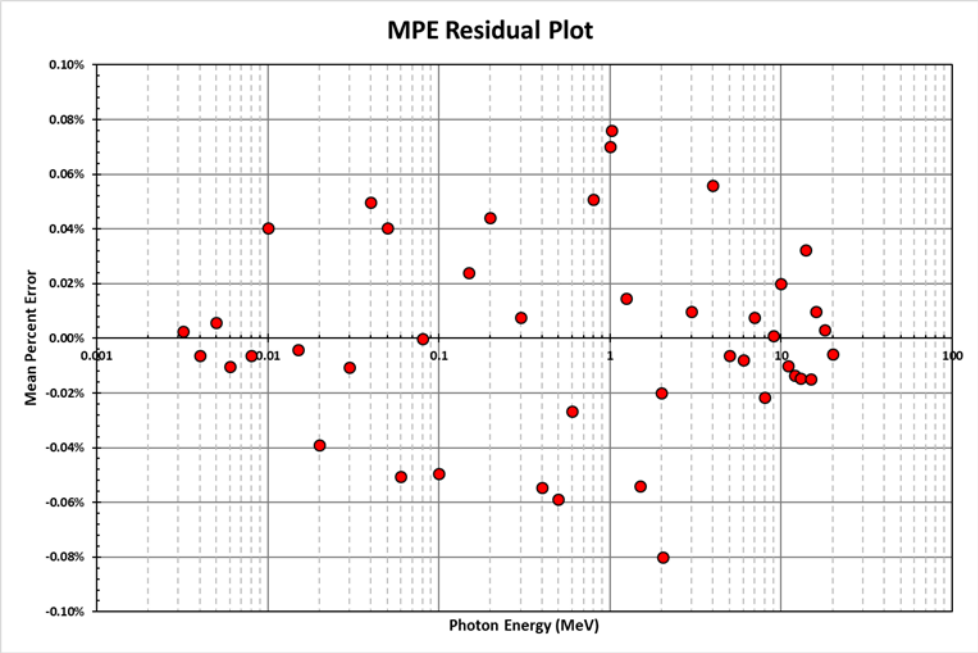

Figure 2-19. The MPE Residual Plot for the Empirical Fit of the Mass Attenuation Coefficient in Air

To demonstrate the photon model's accuracy for an unshielded scenario, 2,713 data points of varying energies and distances along the geometric axis were collected by simulation in MCNP and compared to the lens dose model. Figure 2-20 shows the comparison plot resulting from these estimations. This plot shows only very minor deviations between the observed and predicted values.

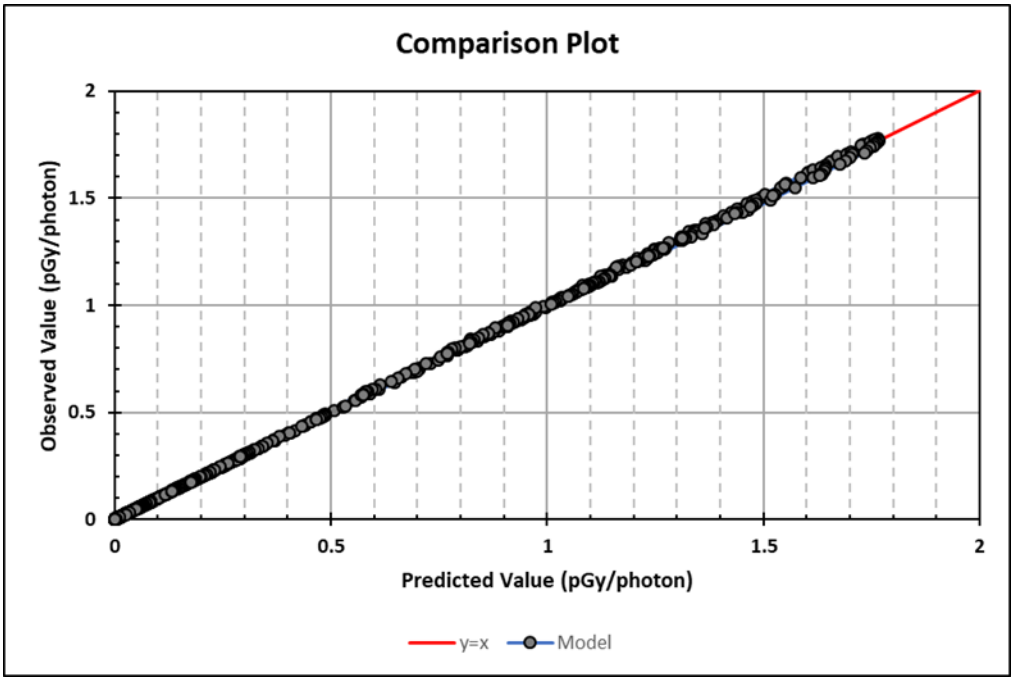

Figure 2-20. Comparison Plot of Photon Model and 2,713 Data Points

Because the model is dependent on two inputs (distance and energy), the MPE can be plotted against both. Figure 2-21 and Figure 2-22 give insight into how well the model predicts the data and where its strongest and weakest points lie. The total MPE is bounded by ±4 percent. Figure 2-21 shows that the largest MPE occurs when photon energy is greater than 8 MeV. This is acceptable because most naturally occurring sources emit photons well under this energy, and so most applications will enjoy the best results. Figure 2-22 shows that the MPE is slightly higher at distances above 800 cm. This is likely due to the weighting scheme used to develop t, u, and v. Because distance plays a role in the probability that a particle will interact inside the target volume, photons starting at these greater distances have a higher uncertainty attached to their estimates and thus are weighted lower.

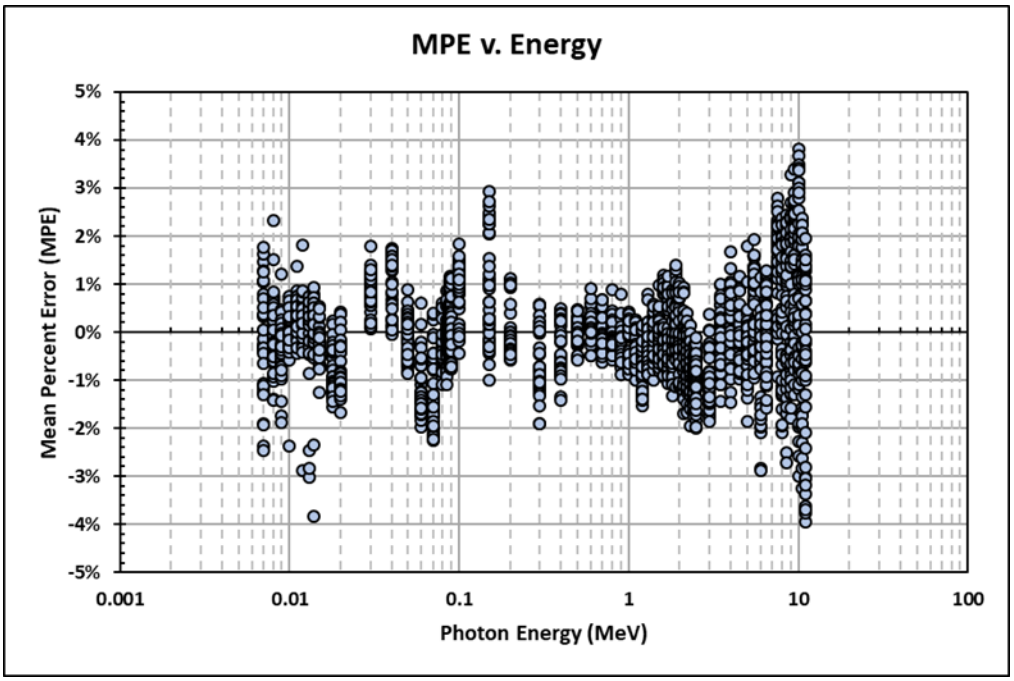

Figure 2-21. The MPE of the Photon Dosimetry Model Plotted Against Photon Energy

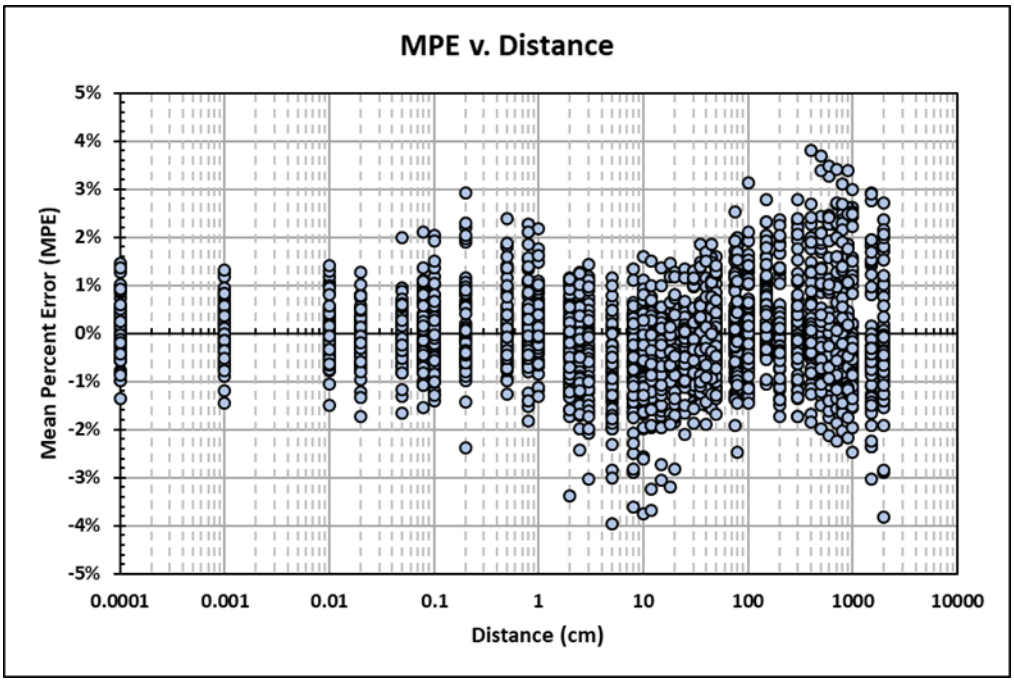

Figure 2-22. The MPE of the Photon Dosimetry Model Plotted Against Distance

To demonstrate the photon model's accuracy for a shielded scenario, a goodness of fit analysis was carried out with the worst fits appearing at 50 keV and 1.25 cm. The MPE is bounded by ±3 percent for all other energies except 60 keV and 11 MeV, which have lower bounds of 5 percent. The comparison plot and residual

plots are shown in Figure 2-23, Figure 2-24, and Figure 2-25.

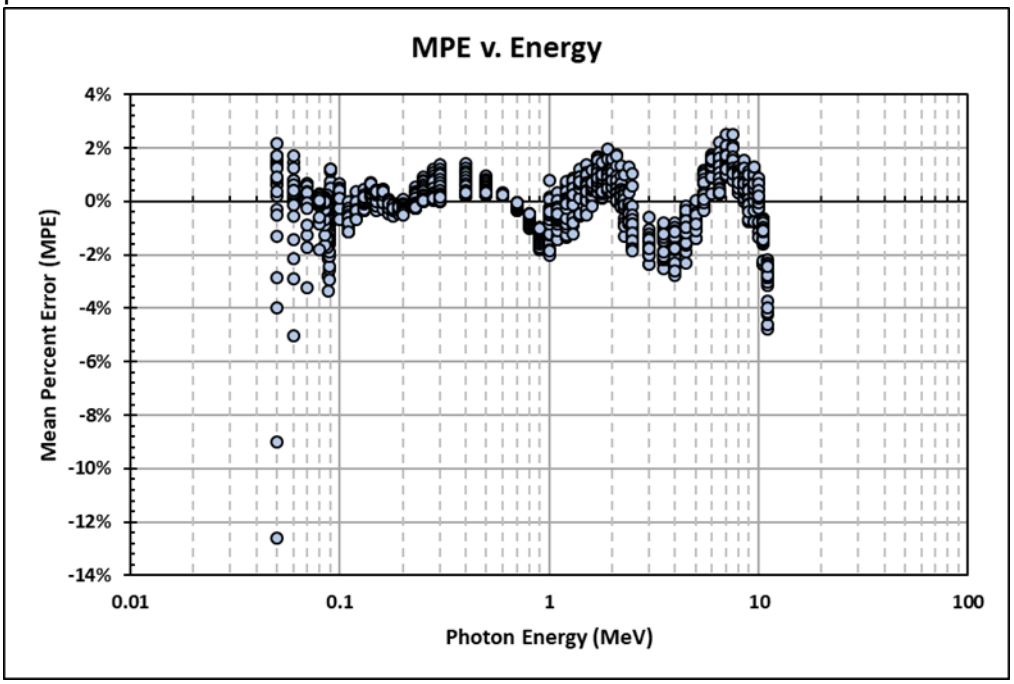

Figure 2-23. Plot of the MPE versus Energy for the Shielded Dose Model

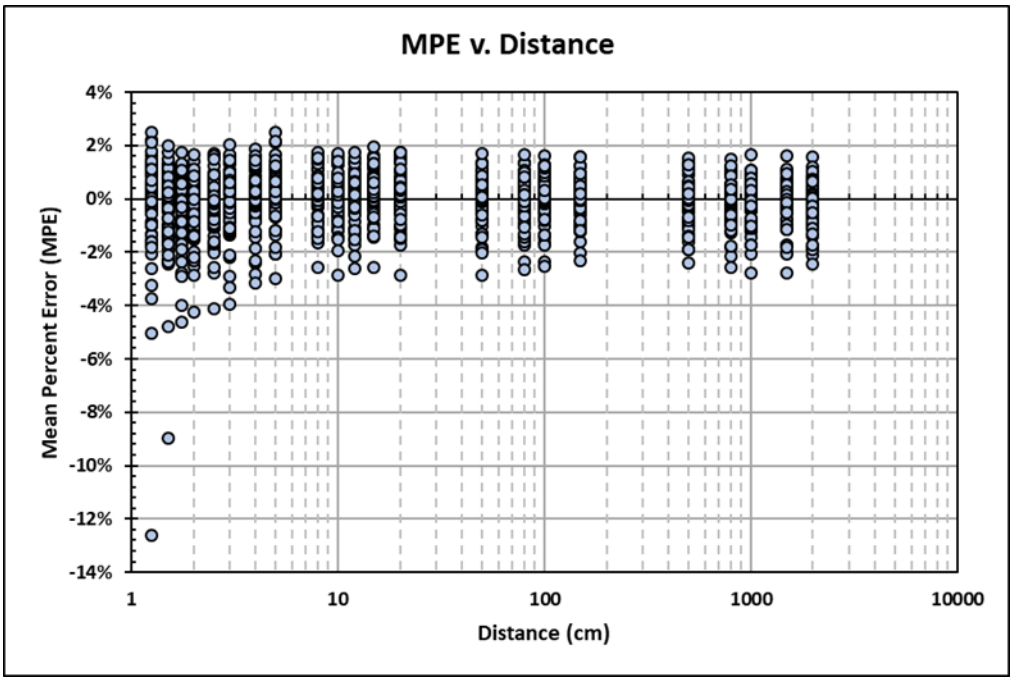

Figure 2-24. Plot of the MPE versus Distance for the Shielded Dose Model

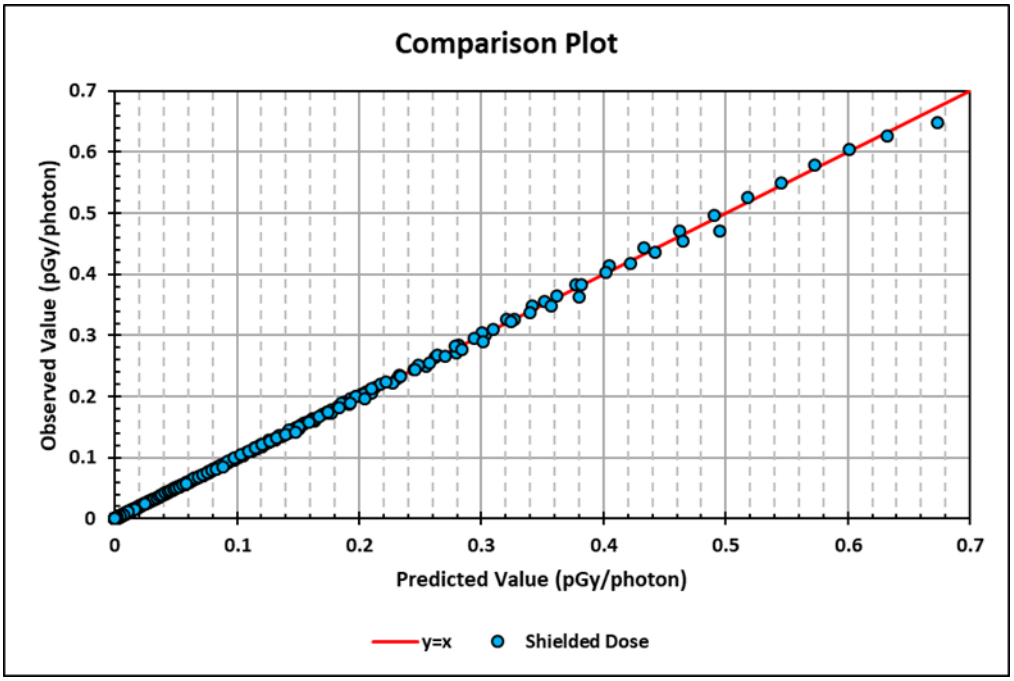

Figure 2-25. Comparison Plot for the Shielded Dose Model

Electrons. Figure 2-26 and Figure 2-27 show the comparison plot between 1,652 data points collected via MCNP simulations and the unshielded electron dosimetry model (Eq. [2.19]). It is apparent that the model fits very well when the observed

dose is greater than about 1x10^{-6} pGy/electron. Some doses below this threshold begin to deviate from the line $y = x$. These deviations are to be expected when air is considered, as air has a significant impact on electron behavior. The farther an electron must travel through air to reach its target, the wider the resulting dose distribution in the target volume.

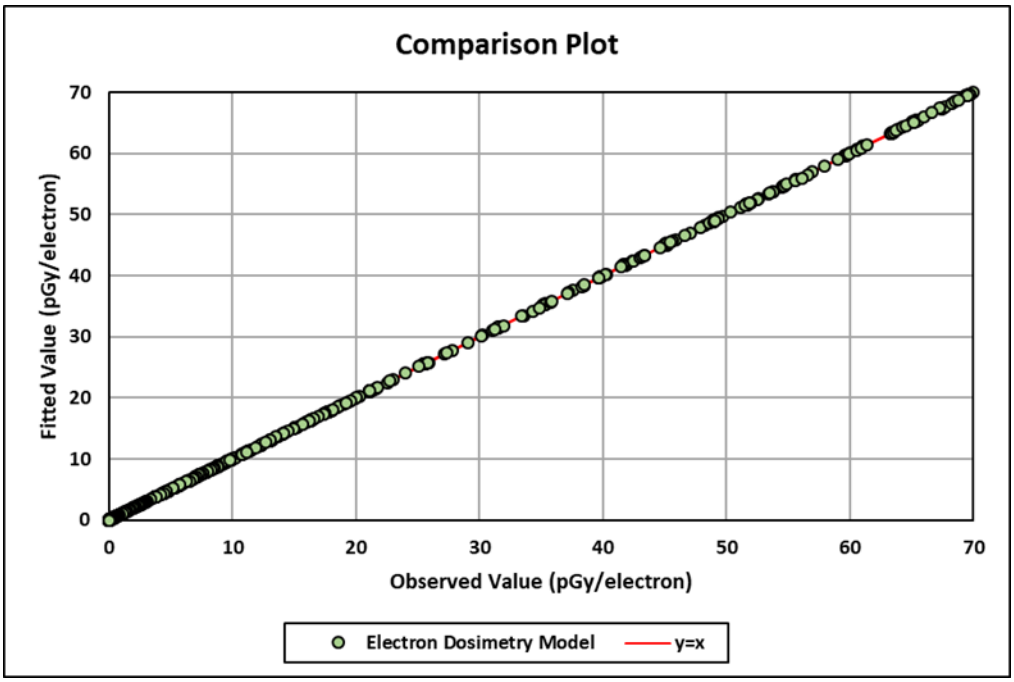

Figure 2-26. Comparison Plot for Unshielded Electrons in Air on Linear Axes

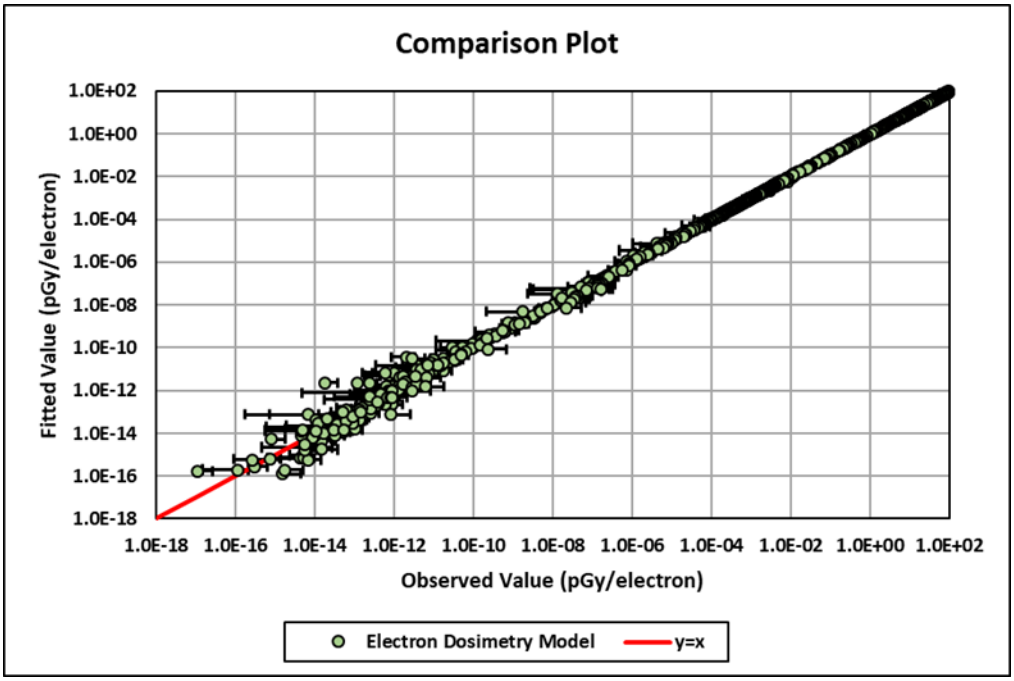

Figure 2-27. Comparison Plot for Unshielded Electrons in Air on Log-Log Axes

For the shielded electron case, parameters for Eq. [2.20] are given for energies above 80 keV and below 11 MeV. Doses at lower energies are negligible and can be taken to be zero. Figure 2-28 (and Figure 2-29) provides the comparison plots for the shielded electron model on linear and log axes. Both plots show excellent agreement. A few points near the lower left in Figure 2-29 appear to deviate significantly from the line $y = x$. These data are not an issue, however, because they are extremely low values of dose and may be considered negligible in most scenarios.

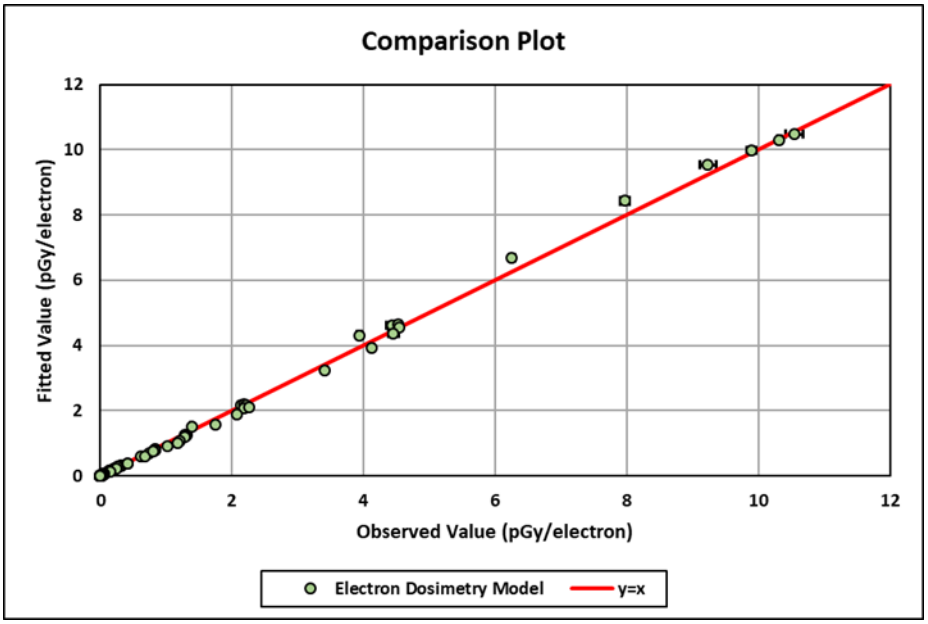

Figure 2-28. Comparison Plot on Linear Axes for Electrons Shielded with Protective Leaded Eyewear

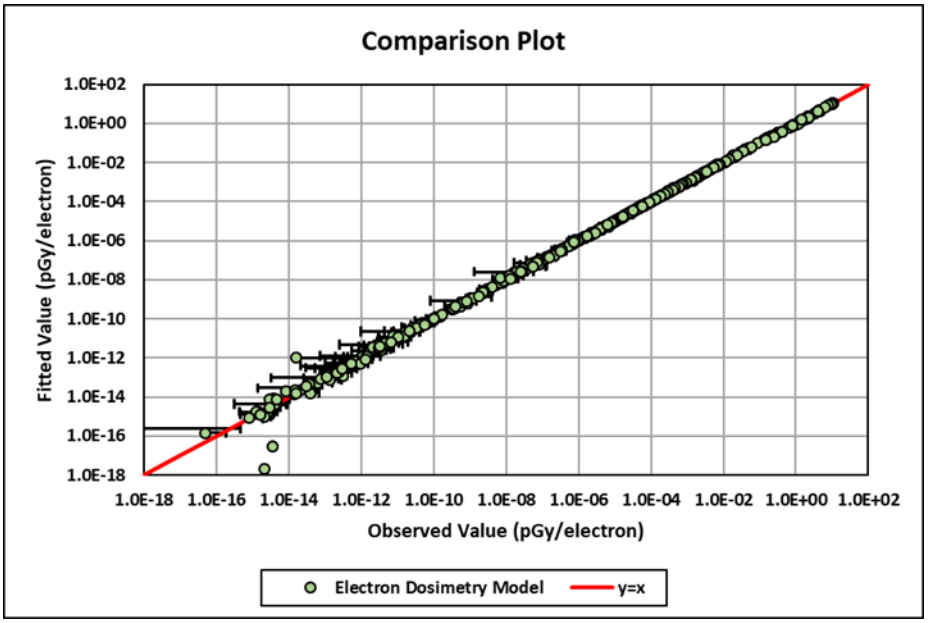

Figure 2-29. Comparison Plot on Log-Log Axes for Electrons Shielded with Protective Leaded Eyewear

Figure 2-30 illustrates the validity of Eq. [2.24] for continuous-energy radiation sources. Three beta sources (P-32, Y-90, and Sr-90) and a 120 kVp X-ray source were modeled in MCNP as continuous energy spectrum point sources. In each example, a source emission rate of 4×10^{10} emissions per second is assumed.

Data collected in MCNP are shown as points while the EyeDose model is shown as a solid line. Error bars represent the 1σ confidence interval and are barely visible. All four examples show excellent agreement, with the largest discrepancies occurring when a beta source was placed more than 100 cm from the eye. Even so, the difference between the observed value and the predicted value is very small.

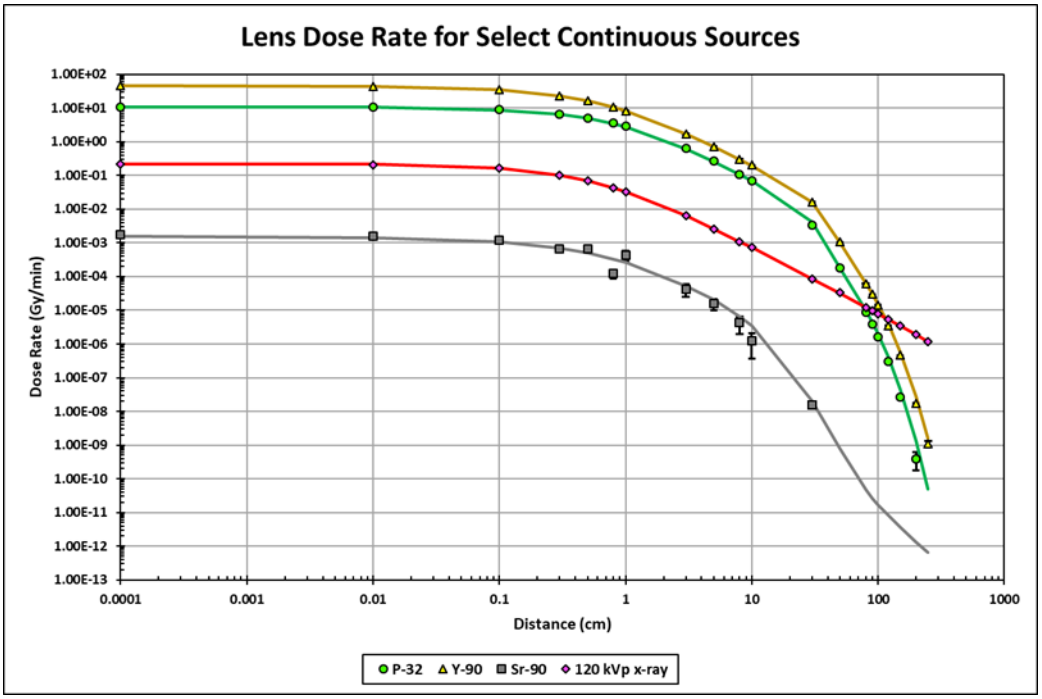

Figure 2-30. Plot of the Lens Dose Rate for Selected Continuous Radiation Point Sources

2.5. SkinDose Comparison

The SkinDose module can be made to loosely simulate the lens. Figure 2-31 provides a cross-sectional view of how SkinDose can be used to simulate the eye. A cylinder, shown in yellow, represents the lens. It is located 0.321 cm below the tissue surface and is 0.43 cm thick. The circular surface area of one face is 1 cm². The blue region represents air, and the peach region represents tissue. This representation does not consider the curvature of the eye, the curvature of the lens, and the varying densities of the tissues of the eye.

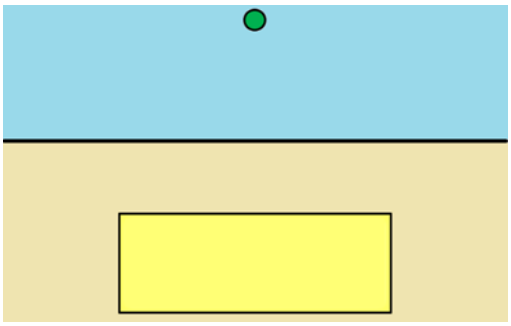

Figure 2-31. Schematic used by SkinDose to Simulate the Lens

Several comparisons were made between this setup in SkinDose, and the EyeDose models. Figure 2-32 shows the results of these comparisons using V+ v2.0. Results are similar in most scenarios, but a few stand out, particularly with a low-energy electron source. For example, the dose from 0.65 MeV electrons is overestimated by EyeDose (compared to SkinDose) at 1 cm and 10 cm, and Co-60 electrons are not reaching the averaging area in SkinDose at any distance. Photons showed good agreement across the board.

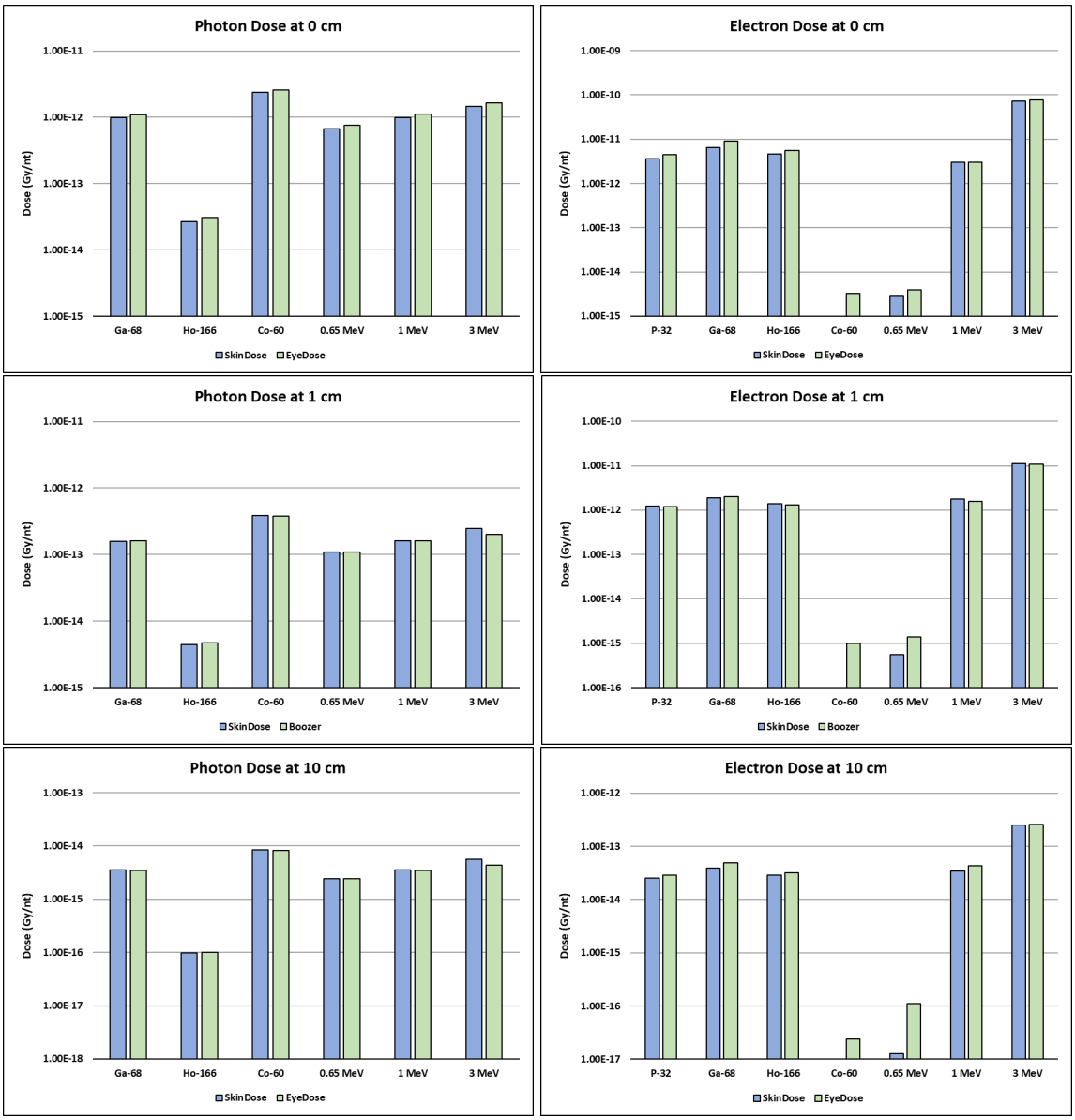

Figure 2-32. Comparison of Calculations Between SkinDose and this Model

2.6. Limitations (Off-Axis Sensitivity Analysis)

A mathematical model of a physical event is only as good as its most uncertain parameter. The EyeDose model essentially assumes the eyeball is focused directly at the source for the entire exposure, an assumption that probably does not hold up in most circumstances. It is therefore desirable to understand how the spatial location of the source relative to the eye can affect dose to the lens. Consider a source that is located off the eye's geometric axis (Figure 2-33). This off-axis source is located a distance r from the eye and makes an angle θ from the geometric axis.

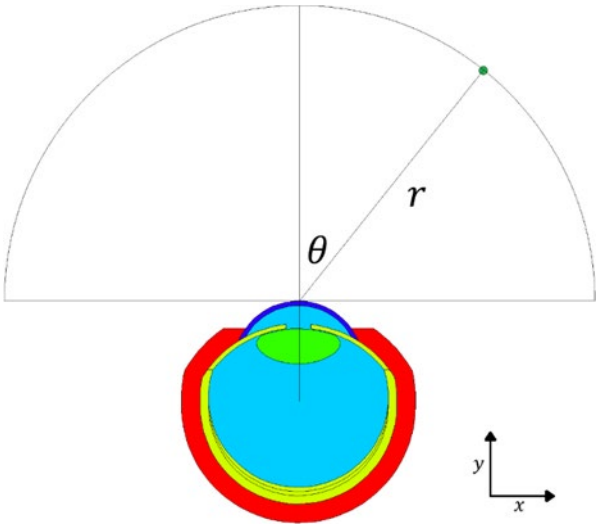

Figure 2-33. Parameter Definitions for an Off-Axis Source.

The following is a rudimentary analysis of the model's sensitivity to source placement. Let $D(r,\theta)$ denote the lens dose for a source located at the point (r,θ) as seen in Figure 2-33. $D(r,\theta)$ was collected from MCNP simulations for r = 0.1, 1, and 10 cm and θ ranging from 0° to 90° in 10° increments. Photon energies considered were 10 keV, 1 MeV, and 10 MeV. Electron energies were 60 keV, 1 MeV, and 3 MeV. A total of 180 simulations were run (90 for each particle type). The head phantom was not modeled. In each simulation, the ratio between the off-axis dose $D(r,\theta)$ and the on-axis dose $D(r,0°)$ was recorded and plotted. Figure 2-34 and Figure 2-35 show the results.

The data clearly indicate that the lens dose depends on the source's spatial location. Furthermore, this dependency is also reliant on the source's energy. The data indicate that the difference between the on-axis and off-axis dose might be within 20 percent provided that θ < 20°.

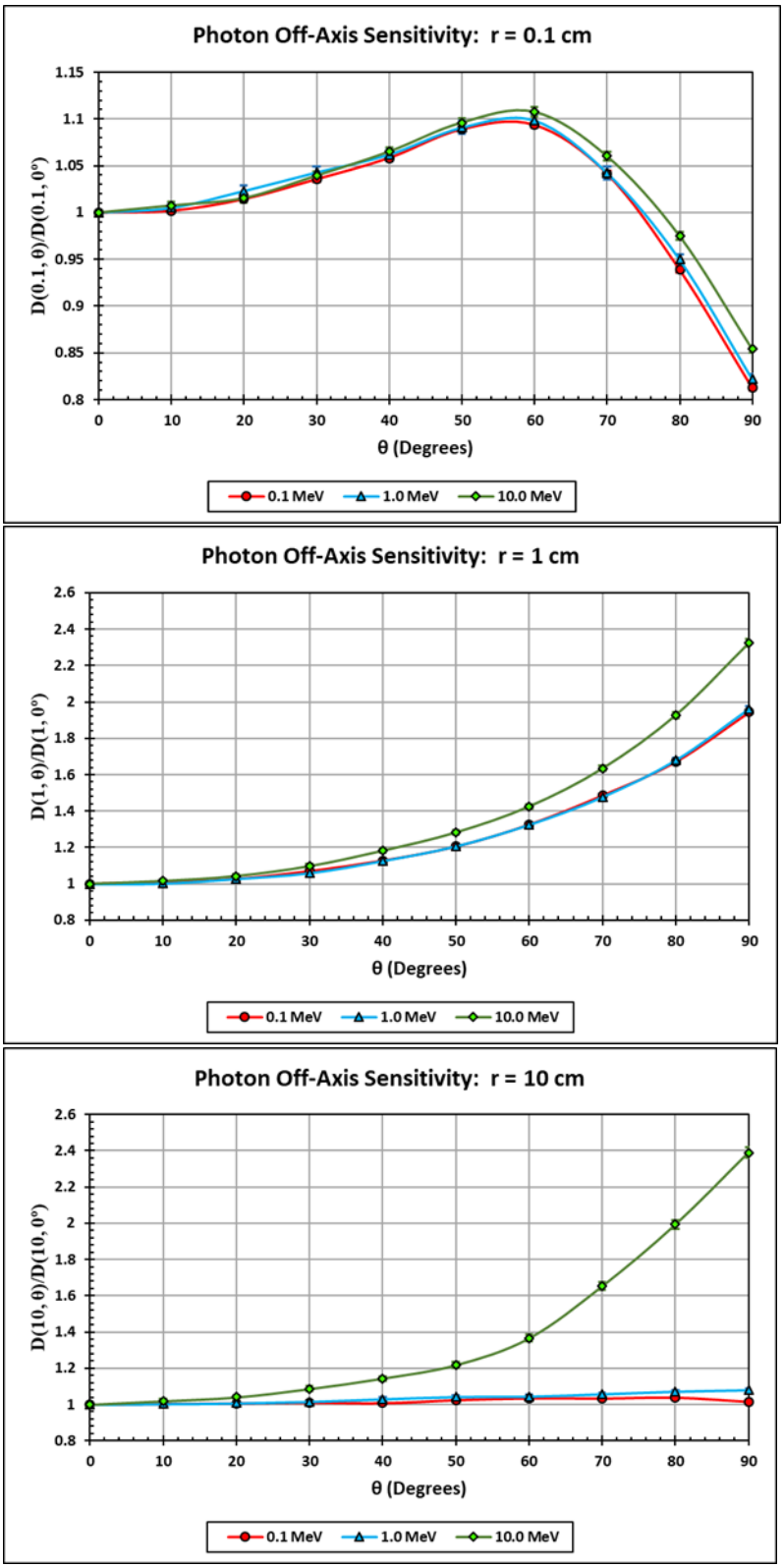

Figure 2-34. $\boldsymbol{D(r,\theta)}$ for Photons with $\boldsymbol{r}$ = 0.1, 1, and 10 cm and $\boldsymbol{\theta}$ Ranging from 0° to 90° in 10° Increments

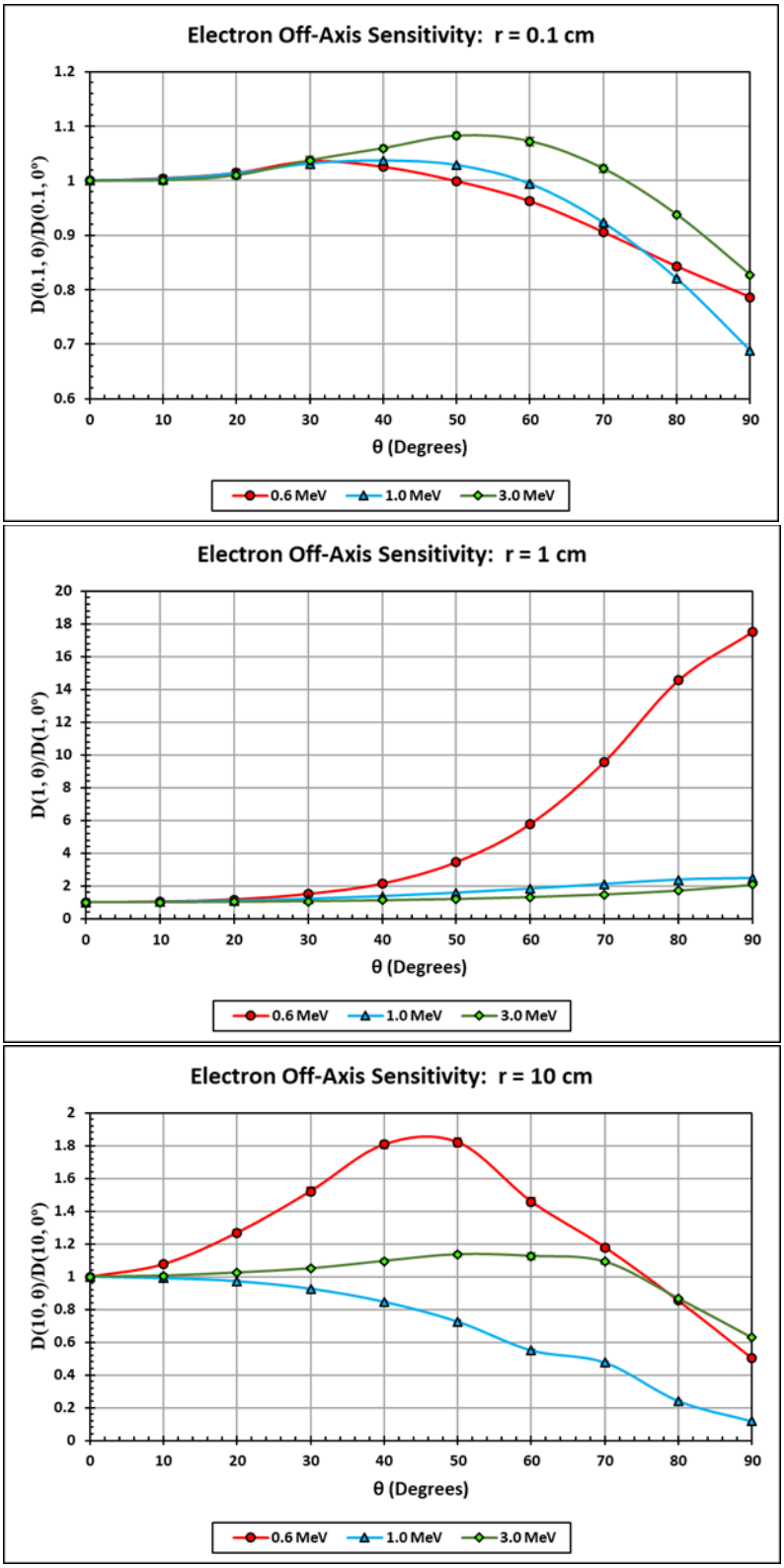

Figure 2-35. $\boldsymbol{D(r,\theta)}$ for Electrons with $\boldsymbol{r}$ = 0.1, 1, and 10 cm and $\boldsymbol{\theta}$ Ranging from 0° to 90° in 10° Increments

3.0 REFERENCES

Attix, F.H. Introduction to Radiological Physics and Radiation Dosimetry. John Wiley & Sons. New York, NY. 1986.

Behrens, R., G. Dietze, and Z. Maria. "Dose conversion coefficients for electron exposure of the human eye lens." *Physics in Medicine and Biology*. 54 (13): 4069-4087. 2009.

Berger, M.J. "Distribution of Absorbed Dose around Point Sources of Electrons and Beta Particles in Water and Other Media." Medical Internal Radiation Dose Committee, Pamphlet No. 7. *Journal of Nuclear Medicine*. Vol. 12, Supplement No. 5. pp. 5–22. 1971.

Boozer, D.L. "A Deterministic Photon and Electron Dosimetry Model for the Lens of the Eye". Dissertation. School of Nuclear Science and Engineering. College of Engineering. Oregon State University. February 2020.

Cross, W.G., N.O. Freedman, and P.Y. Wong. "Tables of Beta-Ray Dose Distributions in Water." AECL 10521, CA9200298. Chalk River Laboratories, Dosimetric Research Branch. Chalk River. Ontario, Canada. 1992.

Hamby, D.M.; Mangini, C.D.; Luitjens, J.M.; Boozer, D.L.; Tucker, Z.G.; Rose, C.T.; Flora, R.S. VARSKIN+ 1.0: A Computer Code for Skin Contamination and Dosimetry Assessments. U.S. Nuclear Regulatory Commission. NUREG/CR-6918, Rev 4. July 2021.

International Commission on Radiological Protection (ICRP). "Reference Man: Anatomical, Physiological, and Metabolic Characteristics." Publication 23. Oxford, England: Pergamon Press. 1975.

International Commission on Radiological Protection (ICRP). "Radionuclide Transformations." Publication 38. Oxford, England: Pergamon Press. 1983.

International Commission on Radiation Protection (ICRP). The 2007 Recommendations of the International Commission on Radiological Protection. ICRP Publication 103. Ann. ICRP 37(2-4). 2007.

International Commission on Radiation Protection (ICRP). "Nuclear Decay Data for Dosimetric Calculations." Publication 107. Ann. ICRP 38 (3). 2008

International Commission on Radiation Protection (ICRP). ICRP Statement on Tissue Reactions / Early and Late Effects of Radiation in Normal Tissues and Organs ─ Threshold Doses for Tissue Reactions in a Radiation Protection Context. ICRP Publication 118. Ann. ICRP 41(1/2). 2012.

International Commission on Radiological Protection (ICRP). Radiological Protection in Therapy with Radiopharmaceuticals. ICRP Publication 140. Ann. ICRP 48(1). 2019.

International Commission on Radiation Units and Measurements (ICRU). "Tissue Substitutes in Radiation Dosimetry and Measurement." ICRU Report 44. Bethesda, MD: International Commission on Radiation Units and Measurements. 1989.

International Commission on Radiation Units and Measurements (ICRU). "Nuclear Data for Neutron and Proton Radiotherapy and for Radiation Protection." ICRU Report 63. Bethesda, MD: International Commission on Radiation Units and Measurements. 2001.

Johns, H.E. and J.R. Cunningham. The Physics of Radiology. 4th Edition. Springfield, IL: Charles C. Thomas. 1983.

Kawrakow, I. and D.W. Rogers. The EGSnrc code system: Monte Carlo simulation of electron and photon transport. *Technical Report* PIRS-701. Ottawa, Canada: National Research Council of Canada. 2000.

Ljungberg, M., S.E. Strand, and M.A. King. Monte Carlo Calculations in Nuclear Medicine, Second Edition. CRC Press. Chapter 10:175–195; 2012.

Los Alamos National Laboratory, X-5 Monte Carlo Team. "MCNP—A General Monte Carlo N-Particle Transport Code, Version 5. LA-CP-03-0245. Los Alamos, NM: LANL. 2003.

National Institute of Science and Technology (NIST). X-Ray Mass Attenuation Coefficients. NISTIR 5632. https://dx.doi.org/10.18434/T4d01F. July 2004.

Radiation Dosimetry Calculations for ICRP and MIRD." CCC–701. Oak Ridge, TN: RSICC. 1995.

Shultis, J.K. and Faw, R.E. Radiation Shielding. American Nuclear Society. ISBN 0-89448-4567. La Grange Park, IL. 2000.

Spackman, D.A. "Design and Analysis of Radiation Shielding Eyewear." Master's Thesis. Oregon State University. Corvallis, OR: 2013.

Spencer, L. V. Theory of Electron Penetration. *Physical Review.* 98: 1597-1615; 1955.

Spencer, L. V. Energy Dissipation by Fast Electrons. *National Bureau of Standards Monograph 1*; 1959.

U.S. Department of Health and Human Services (HHS). Radiation Emergency Medical Management (REMM). https://remm.hhs.gov (website last updated on January 19, 2023). 2023.

U.S. Nuclear Regulatory Commission. Traub, R.J., W.D. Reece, R.I. Scherpelz, and L.A. Sigalla. "Dose Calculation for Contamination of the Skin Using the Computer Code VARSKIN." NUREG/CR–4418. Washington, DC: NRC. 1987.

U.S. Nuclear Regulatory Commission. Reece, W.D., S.D. Miller, and J.S. Durham. "SADDE (Scaled Absorbed Dose Distribution Evaluator), A Code to Generate Input for VARSKIN." NUREG/CR–5276. Washington, DC: NRC. 1989.

U.S. Nuclear Regulatory Commission. Durham, J.S. "VARSKIN Mod 2 and SADDE Mod 2: Computer Codes for Assessing Skin Dose from Skin Contamination." NUREG/CR-5873, PNL-7913. Washington, DC: NRC. 1992.

U.S. Nuclear Regulatory Commission. Durham, J.S. "VARSKIN 3: A Computer Code for Assessing Skin Dose from Skin Contamination." NUREG/CR-6918. Washington, DC: U.S. Nuclear Regulatory Commission. 2006.

U.S. Nuclear Regulatory Commission. Hamby, D.M., Lodwick, C.J., Palmer, T.S., Reese, S.R., Higley, K.A. "VARSKIN 4: A Computer Code for Skin Contamination Dosimetry." NUREG/CR-6918, Rev 1. Washington, DC: U.S. Nuclear Regulatory Commission. 2011.

U.S. Nuclear Regulatory Commission. Hamby, D.M., Mangini, C.D., Caffrey, J.A., Tang, M. "VARSKIN 5: A Computer Code for Skin Contamination Dosimetry." NUREG/CR-6918, Rev 2. Washington, DC: U.S. Nuclear Regulatory Commission. 2014.

U.S. Nuclear Regulatory Commission. Hamby, D.M., Mangini, C.D. "VARSKIN 6: A Computer Code for Skin Contamination Dosimetry." NUREG/CR-6918, Rev 3. Washington, DC: U.S. Nuclear Regulatory Commission. 2018.